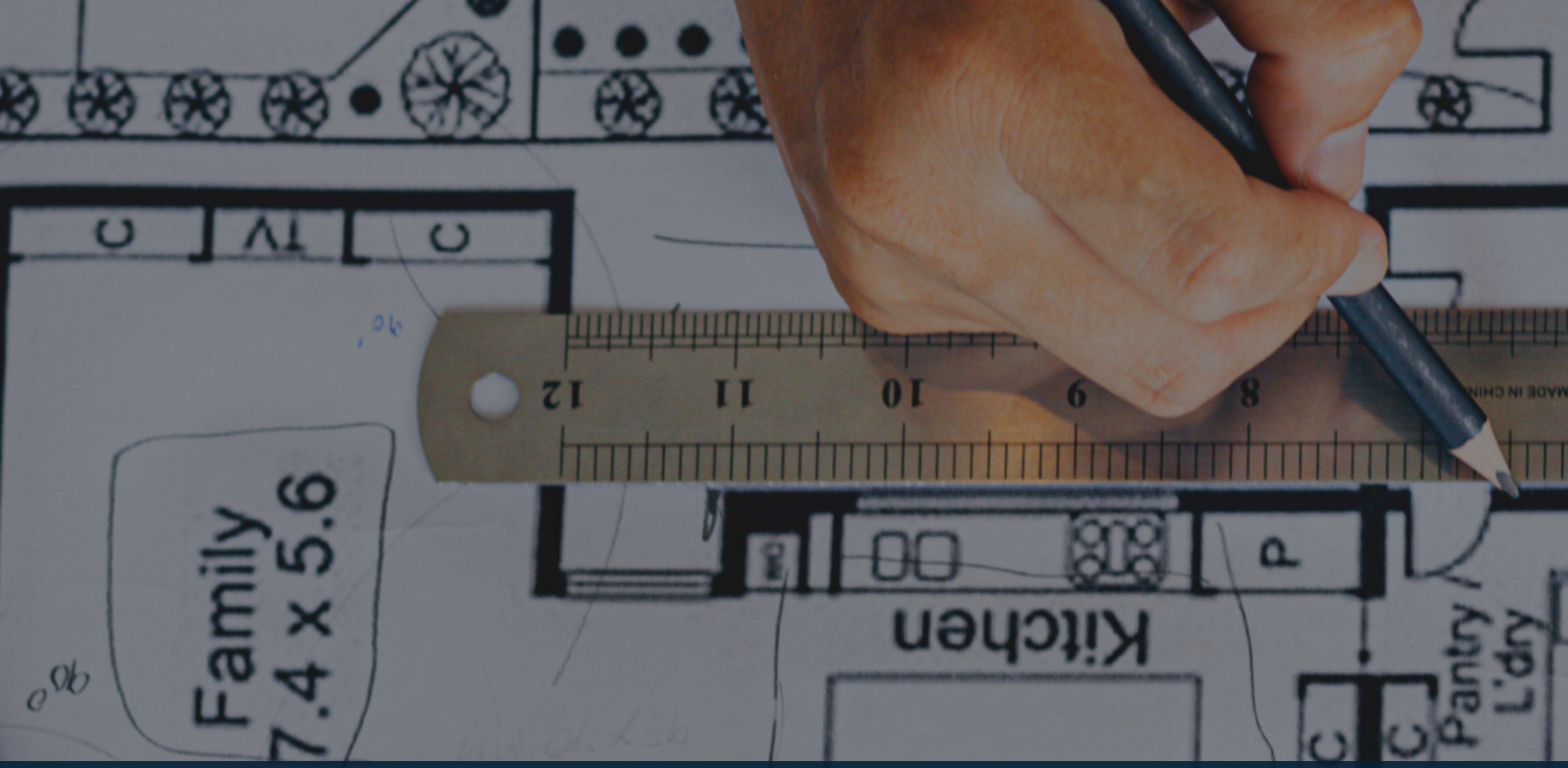

www.icens.eu

ICENS

8TH INTERNATIONAL CONFERENCE ON ENGINEERING AND NATURAL SCIENCES

BOOK OF PROCEEDINGS

May 18-22, 2022

Organized by

CSUN

University of CINCINNATI

Partners

CNR GROUP

8th INTERNATIONAL CONFERENCE ON ENGINEERING AND NATURAL SCIENCES (ICENS)

ISBN 978-605-81426-1-9
ISSN 2687-2447

PROCEEDINGS OF THE
8th INTERNATIONAL CONFERENCE ON ENGINEERING AND NATURAL SCIENCES (ICENS)
MAY 18 to 22, 2022 in ISTANBUL, TURKEY (ONLINE CONFERENCE)

Edited by

Prof. Dr. Özer Çınar

Published by:

info@icens.eu
www.icens.eu
www.cnrgroup.eu

CNR Group Laboratuvar ve Arge Hizmetleri Sanayi Ticaret Limited Şirketi Çifte Havuzlar Mah., Eski Londra Asfaltı Cad., Kuluçka Mrk., A1 Blok, 151/1C, Iç Kapı No:1 B-20, Esenler / Istanbul, 34220

ISBN 978-605-81426-1-9

ISSN 2687-2447

SCIENTIFIC COMMITTEE

1. Prof. Dr. Adisa Parić - University of Sarajevo - Bosnia and Herzegovina
2. Prof. Dr. Aleksandar Dimitrov - Ss. Cyril and Methodius University - North Macedonia
3. Prof. Dr. Alexander Golub - National University of Kyiv-Mohyla Academy - Ukraine
4. Prof. Dr. Alexander Litvinenko - National University of Food Technologies (Kyiv) - Ukraine
5. Prof. Dr. Alit Ibraimi - University of Tetova - North Macedonia
6. Prof. Dr. Anita Grozdanov - Ss. Cyril and Methodius University - North Macedonia
7. Prof. Dr. Asif Šabanović – International University of Sarajevo - Bosnia and Herzegovina
8. Prof. Dr. Bekir Erol Ak - Harran University - Turkey
9. Prof. Dr. Cem Şensöğüt - Dumlupınar University - Turkey
10. Prof. Dr. Christos Douligeris - University of Erlangen-Nurnberg - Germany
11. Prof. Dr. Dragutin T. Mihailović - University of Novi Sad - Serbia
12. Prof. Dr. Evgeniy Shtefan - National University of Food Technologies (Kyiv) - Ukraine
13. Prof. Dr. Falko Dressler - University of Paderborn - Germany
14. Prof. Dr. Houssam Toutanji – Western Michigan University - USA
15. Prof. Dr. Ian F. Akyıldız – Georgia Institute of Technology - USA
16. Prof. Dr. İsmail Usta - Marmara University - Turkey
17. Prof. Dr. Kateryna Derevska - National University of Kyiv-Mohyla Academy - Ukraine
18. Prof. Dr. Liljana Gavrilovska - Ss Cyril and Methodius University - Macedonia
19. Prof. Dr. Lukman Thalib - Qatar University - Qatar
20. Prof. Dr. M. Asghar Fazel – University of Environment - Iran
21. Prof. Dr. Mikhailov Volodymyr - Taras Shevchenko National University of Kyiv - Ukraine
22. Prof. Dr. Mykola Glybovets - National University of Kyiv-Mohyla Academy - Ukraine
23. Prof. Dr. Muammer Koç - Hamad bin Khalifa University - Qatar
24. Prof. Dr. Nadia Bilko - National University of Kyiv-Mohyla Academy - Ukraine
25. Prof. Dr. Özer Çınar – Yıldız Technical University - Turkey
26. Prof. Dr. Perica Paunovik - Ss. Cyril and Methodius University - Macedonia
27. Prof. Dr. Rifat Škrijelj – University of Sarajevo - Bosnia and Herzegovina
28. Prof. Dr. Samir Đug - University of Sarajevo - Bosnia and Herzegovina
29. Prof. Dr. Tanju Karanfil – Clemson University - USA
30. Prof. Dr. Ümit Alver – Karadeniz Technical University - Turkey
31. Prof. Dr. Wolfgang Gerstacker - University of Erlangen-Nurnberg - Germany
32. Prof. Dr. Vladyslav Sukhenko - National University of Life and Environmental Sciences of Ukraine (Kyiv) - Ukraine
33. Prof. Dr. Vullnet Ameti - University of Tetova - North Macedonia
34. Prof. Dr. Yılmaz Yıldırım - Bülent Ecevit University - Turkey
35. Prof. Dr. Yousef Haik - Hamad bin Khalifa University - Qatar
36. Assist. Prof. Dr. Abdelwahab Tahsin - Eqyptian Russian University - Egypt
37. Assist. Prof. Dr. Agon Memeti - University of Tetova - North Macedonia
38. Assoc. Prof. Dr. Alaa Al Hawari - Qatar University - Qatar
39. Assist. Prof. Dr. Arianit Reka - University of Tetova - North Macedonia
40. Assoc. Prof. Dr. Fatih Ungan - Cumhuriyet University - Turkey
41. Assoc. Prof. Dr. Izudin Dzafic - International University of Sarajevo - Bosnia and Herzegovina
42. Assoc. Prof. Dr. Kateryna Syera - National University of Life and Environmental Sciences of Ukraine (Kyiv) - Ukraine
43. Assist. Prof. Dr. Muhamed Hadziabdic - International University of Sarajevo - Bosnia and Herzegovina
44. Assoc. Prof. Dr. Nusret Drešković - University of Sarajevo - Bosnia and Herzegovina
45. Assoc. Prof. Dr. Polina Vakuliuk - National University of Kyiv-Mohyla Academy - Ukraine
46. Assoc. Prof. Dr. Senija Tahirovic - International University of Sarajevo - Bosnia and Herzegovina
47. Assoc. Prof. Dr. Victor Karamushka - National University of Kyiv-Mohyla Academy - Ukraine
48. Assoc. Prof. Dr. Victoria Konovalova - National University of Kyiv-Mohyla Academy - Ukraine
49. Assoc. Prof. Dr. Yuriy Kravchenko - National University of Life and Environmental Sciences of Ukraine (Kyiv) - Ukraine
50. Assist. Prof. Dr. Fatih Taktak - Uşak University - Turkey
51. Assist. Prof. Dr. Fouzi Tabet - German Biomass Research Center - Germany
52. Assist. Prof. Dr. Haris Gavranovic - International University of Sarajevo - Bosnia and Herzegovina
53. Assist. Prof. Dr. Hüseyin Pehlivan - Gebze Technical University - Turkey
54. Assist. Prof. Dr. Sasan Rabieh - Shahid Beheshti University - Iran
55. Assist. Prof. Dr. Ševkija Okerić - University of Sarajevo - Bosnia and Herzegovina
56. Assist. Prof. Dr. J. Amudhavel - VIT Bhopal University - India
57. Dr. Zsolt Hetesi - National University of Public Service, Budapest - Hungary
58. Dr. Zsolt T. Németh - National University of Public Service, Budapest - Hungary

ORGANIZATION COMMITTEE

Chairman of the Conference

Prof. Dr. Özer Çınar – Yıldız Technical University

Members of the Committee

Prof. Dr. Ümit Alver (Co-Chairman) - Karadeniz Technical University - Turkey
Assist. Prof. Dr. Sasan Rabieh - Shahid Beheshti University - Iran
Alma Ligata - Zenith Group - Bosnia and Herzegovina
Ismet Uzun - Zenith Group - Bosnia and Herzegovina
Musa Kose - Zenith Group - Bosnia and Herzegovina

WELCOME TO ICENS 2022

On behalf of the organizing committee, we are pleased to announce that the 8th International Conference on Engineering and Natural Sciences (ICENS 2022) held from May 18 to 22, 2022 in Istanbul, Turkey. ICENS provides an ideal academic platform for researchers to present the latest research findings and describe emerging technologies, and directions in Engineering and Natural Sciences issues. The conference seeks to contribute to presenting novel research results in all aspects of Engineering and Natural Sciences. The conference aims to bring together leading academic scientists, researchers and research scholars to exchange and share their experiences and research results about all aspects of Engineering and Natural Sciences. It also provides the premier interdisciplinary forum for scientists, engineers, and practitioners to present their latest research results, ideas, developments, and applications in all areas of Engineering and Natural Sciences. The conference will bring together leading academic scientists, researchers and scholars in the domain of interest from around the world. The scientific program will focus on current advances in the research, production and use of Engineering and Natural Sciences with particular focus on their role in maintaining academic level in Engineering and Applied Sciences and elevating the science level. The conference's goal will to provide a scientific forum for all international prestige scholars around the world and enable the interactive exchange of state-of-the-art knowledge. The conference will focus on evidence-based benefits proven in clinical trials and scientific experiments.

Best regards,
Prof. Dr.Özer ÇINAR

ICENS 8TH INTERNATIONAL CONFERENCE ON ENGINEERING AND NATURAL SCIENCE
May 18-22 2022 Istanbul (Hybrid Event)

CONTENT	Country	Page
A Study of a Blasting Operation in Open Pit Mine With GPSS/H Simulation Program	Turkey	1
Lateral strength-based seismic evaluation of an unreinforced masonry building	Turkey	5
The Forecast of Value of Lost Load in Slovenia	Slovenia	13
Review of the reliability standards in EU electric power system	Slovenia	19
An Investigation on Plan and Facade Characteristics of High-Rise Buildings	Turkey	24
Effect of Nozzle Tip Geometry on Drop Diameter Falling Down String	Turkey	29
Optimization of the Cooling Parameters of a 250 kW PMSM by Taguchi Method	Turkey	35
Comparative Life Cycle Assessment of Metalworking Processes in Shipyards	Turkey	45
Numerical study of heat transfer of a battery pack consisting of plate-shaped lithium-ion batteries connected to the solar system in an air channel in the presence of PCM	Turkey	50

ICENS 8TH INTERNATIONAL CONFERENCE ON ENGINEERING AND NATURAL SCIENCE
May 18-22 2022 Istanbul (Hybrid Event)

A Study of a Blasting Operation in Open Pit Mine With GPSS/H Simulation Program

***Necmettin Cetin*[1]**

Abstract

The economic analysis and the use of explosives is an important part of blasting operations in open pit mining. Explosives are energy and the efficient use of this energy is a major factor in keeping rock blasting costs under control. The degree of fragmentation and movement obtained is directly related to the amount of explosives used in operation and the delay array sequencing of firing blasthole. For economic reasons, blasting must be both well planned and be accurately executed using minimum amount of explosives. If the blast sequence is correct, less explosives will be required at a single time. In this study, a simulation model is developed by using GPSS/H simulation software program for a small open pit mine with 11 blasthole operation drilled out at a given array pattern to determine the out of sequence firing (OOSF) and crowding as ms delays by varying the scatter in mean delay time while assuming a predefined value for crowding as ms delay. The simulation results and the interpretations of them for a given mine site provides the optimal sequencing and the scatter of the selected blasting agent.

Keywords: Open Pit Mining, Blasting Patterns, Discrete-Event System Simulation, GPSS/H Software

1. INTRODUCTION

Drilling and blasting are two of the major unit operations in most open pit mines. The main goal for these operations is to optimize rock fragmentation that may cost as high as 25-30 % of the total operating cost in open pit mining. Efficient blast design along with proper choice of explosives can produce better fragmentation with associated lower operating cost compared to the blast designs and explosives under adverse conditions. Delay patterns and varying the blasthole array to fit the natural excavation topography allow for more efficient use of the explosive energy in a blast. Benches may be designed and carried out with more than one face so that simple blasting patterns can be used to remove the rock materials. [1].

A face (or bench in an open pit mine) about to be blasted consists of numerous holes filled with powder (or suitable blasting agent). The holes are blasted in sequence to allow for maximum fragmentation and detonation. For example, if the holes were drilled in concentric circles, the sequence of the blast would be from the innermost ring to the outer ring. Each of the holes in each circle would ideally have the same delay. To ensure this sequencing, delay detonators are used. The length of this delay is given by the manufacturer's specification in milliseconds (ms).

For economic reasons, the blast must be both well planned and be accurately executed using the minimum amount of explosives. If the blast sequence is correct, less explosives are required at a single time.

Typical delays, as given by manufacturers, might be for 200 ms, 300 ms, 1500 ms etc. However, in practice, these delays tend to be average values and the actual delay times are stochastically distributed. In this example, the delay times will be assumed to be estimated from a normal distribution. Figure 1 shows a typical face about to be blasted. It is of concern both the holes are fired in proper sequence and that they do not fire too close in sequence. If the holes fire out of sequence, this is known as "Out-of-Sequence-Firing" (OOSF), if they fire too close together, this is known as "Crowding". Figure 2 shows an arrangement of a few holes. Those numbered 1, are to be donated at the same time and so have a delay of 200 ms. those numbered 2 are to be fired next and they have a delay of 300 ms.

[1] *Corresponding author: Kutahya Dumlupinar University, Department of Mining Engineering, 43100, Kutahya / Turkey.*
necmettin.cetin@dpu.edu.tr

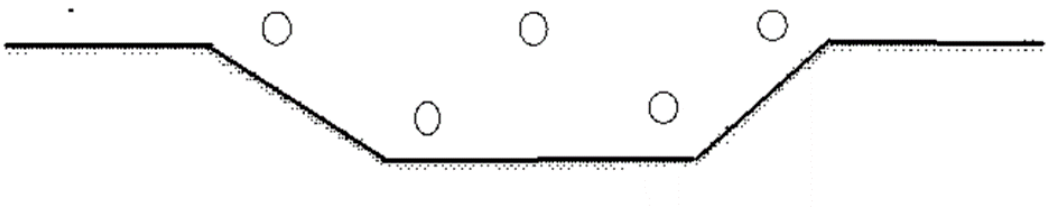

Figure 1. A typical face to be blasted of firing for holes

Figure 2. Arrangement for firing of blast holes

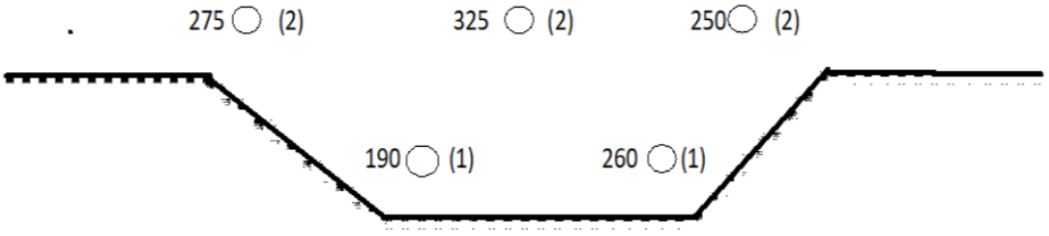

Figure 3. Actual delay times for blast holes

2. MATERIAL AND METHOD

The listing of the program is given as MINEBLAST.GPS. GPSS/H is a discrete-event systems simulation language widely used by many academicians and commercial users and it uses process-interaction approach to modelling. The modeler specifies the sequence of events separated by lapses in time which describes the manner in which objects flow through a system. Models are developed in text files in GPSS/H and compiled into memory and executed [2]. It is considered in this study a case study problem which consists of a series of shots as given by the arrangement in Figure 4.

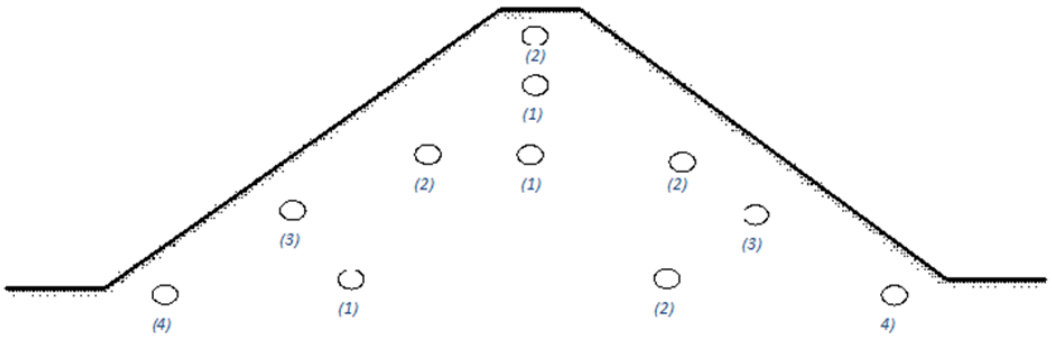

Figure 4. Arrangement of firing for sample holes

As can be seen, there are 11 holes to fire in 4 sequence which are numbered (1), (2), (3) and (4). The planned sequence is first the three holes labelled (1), next the four holes labeled (2), then (3) with two holes, and finally, (4) with 2 holes. The delay times are sequentially, 200 ms, 400 ms, 600 ms and 1000 ms for this sequence.

Actual delay time is assumed to be mean time with a standard deviation of 12 %. If blasting takes place in sequence, but within 30 ms of another hole, crowding is assumed to take place. Because of the statistical nature of the delay times, OOSF and crowding will only take place in subsequent hole blasts, i.e. between holes (1) and (2), (2) and (3) and (3) and (4).

3. RESULTS AND DISCUSSION

The simulation was done for 200 simulated blasts [3]. There were 11 holes and, because of their arrangement, each time a simulation was done, there had to be 24 tests for OOSF and crowding. This first sequence (1) consisted of 3 holes. Their blast times were compared to the second sequence of holes (2) consisting of 4 holes. There were 12 tests done here. However, the next sequence (2) for 8 total comparisons. Finally, sequence (4) consisted of 2 holes and each of these was compared to the sequence (3). There were 4 such comparisons. Thus the total of 24 (12 + 8 + 4). The simulation was performed for varying values of the scatter. 1000 simulated blasts were performed. The mean delay times are as shown in Figure 3 and the standard deviations were taken starting at 9 % of these values. Crowding was assumed to take place if the delay was 30 ms or less. The simulation was the repeated with std. dev. increased by 1 % until it was 20 % of the mean. Input values and prompt are:

Input the time for crowding as ms delay

<< 30>>

How many blasts to simulate for

<<1000>>

Input the scatter as a percent

<<9>>

The simulation results are given in Table 1. The interpretation of the results depend on the particular mining situation and how many OOSF's are allowed. If these are to be no more than, say, 0.5 %, then the detonators need to have a standard deviation of less than 13 % of the mean as this gave 100 OOSF's. There were 24.000 possible OOSF's and 0.5 % of this is 120. For a standard deviation of 14% of the mean, there were 140 OOSF's.

Table 1. Results of Simulation for Case Study Problem

% Scatter Std. Dev.	Out of Sequence Firings	Crowding
9	5	20
10	15	32
11	35	62
12	60	77
13	100	89
14	140	110
15	182	133
16	242	139
17	298	164
18	255	195
19	412	233
20	484	277

4. CONCLUSIONS

A small case study example problem is presented for blasting pattern in open pit mine where a series of shots as given by the arrangement. Drilling and blasting practices used in many open pit mines are mostly designed by the intensive grade-control practices that have developed as a result of complex grade distributions found in these ore bodies.

REFERENCES

[1]. S. M. Benett and J. R. Sturgul, "*A computer Simulation Model of a Surface Blast*", Int. Jour. of Surface Mining, Vol.2 No.2, Belkema Publ. 1989.
[2]. T. J. Schriber, An Introduction to Simulation Using GPSS/H, John Wiley &Sons, 1990.
[3]. J. Banks, J. S. Carson, B. L. Nelson and D. M. Nicol, Discrete-Event System Simulation, 5th Ed. Pearson Education. Publ., 2010

ICENS 8TH INTERNATIONAL CONFERENCE ON ENGINEERING AND NATURAL SCIENCE
May 18-22 2022 Istanbul (Hybrid Event)

Lateral strength-based seismic evaluation of an unreinforced masonry building

Necibe Vatansever Erol[1], Ahmet Vefa Orhon[2], Taner Ucar[3]

Abstract

Unreinforced concrete masonry (URM) buildings located in seismic areas still constitute an important portion of the residential building stock of Turkey. A significant amount of these buildings is designed according to allowable stress criteria of the 2007 version of Turkish Earthquake Code. However, seismic design philosophy, as well as seismic performance assessment, of URM buildings tends to focus on the lateral strength of URM walls and it is also adopted to the current version of Turkish Earthquake Code. Accordingly, the seismic performance of a URM building designed based on the theory of allowable stress is a significant concern. In this study, the seismic performance of a two-story URM building is investigated based on the ultimate strength method. The case study building is primarily designed in accordance with seismic requirements of the 2007 version of Turkish Earthquake Code. Subsequently, lateral strength-based seismic performance assessment of the same building is performed. The earthquake demand is represented by a 5%-damped elastic acceleration design spectrum and the lateral strengths of URM walls are calculated in accordance with provisions of the current Turkish Earthquake Code. All analyses are conducted on a very detailed three-dimensional finite element model (FEM) of the building. The results have shown that the lateral strength capacities of some URM walls located on the ground floor are exceeded, whereas none of the URM walls on the upper floor reach their capacities. As a result, collapse prevention performance level is not achieved.

Keywords: URM building, seismic evaluation, FEM, allowable stress, lateral strength.

1. INTRODUCTION

Seismic hazards posed by existing URM buildings have long been recognized and reported after past earthquakes occurred in active seismic zones in the world, as well as in Turkey. URM buildings are likely to suffer extensive damage and could partially or completely collapse during major seismic events. Since mechanical properties of masonry components are more complicated than their modern counterparts and due to several other reasons such as workmanship employed in masonry construction, poor construction quality, lack of maintenance, an adequate prediction of the seismic behavior of URM buildings is one of the fundamental topics in earthquake engineering. Although URM is one of the oldest building construction techniques, the seismic behavior of those types of buildings is still one of the least understood.

Typical URM buildings in Turkey have brick walls with no steel reinforcing bars embedded within them. They are commonly located in rural regions to be used for residential purposes. Some of these buildings have structural deficiencies due to inappropriate seismic design whereas the others are constructed ignoring the code requirements. Moreover, before the 2007 version of Turkish Earthquake Code (TEC) [1], earthquake analysis of URM buildings is not imposed when both masonry material and geometric requirements of the code are satisfied. The most significant improvement in the seismic design of masonry structures in Turkey is the addition of simple procedures for the calculation of vertical compression and shear stresses developed in masonry walls subjected to earthquake loading. When the current version of the code, Turkey Building Earthquake Code (TBEC) [2], was published, the seismic design of URM buildings is refined from allowable stress theory to ultimate strength philosophy. It is quite clear that URM buildings designed in accordance with the stress-based code requirements are expected to satisfy the lateral strength-based criteria of TBEC.

[1] *Dokuz Eylul University, Department of Architecture, 35390, Buca/Izmir, Turkey. necibe.vatansever@deu.edu.tr*

[2] *Dokuz Eylul University, Department of Architecture, 35390, Buca/Izmir, Turkey. vefa.orhon@deu.edu.tr*

[3] *Corresponding author: Dokuz Eylul University, Department of Architecture, 35390, Buca/Izmir, Turkey. taner.ucar@deu.edu.tr*

Several studies have been conducted on seismic behavior and design of URM buildings. Some of these studies have been focused on developing reliable modeling techniques for seismic analysis and risk assessment of URM buildings [3]–[10]. Earthquake analysis [11]–[14], as well as seismic performance and risk assessment [15]–[24], of URM buildings, have been widely studied. Since URM buildings are characterized by a high seismic vulnerability, seismic retrofitting of these buildings always remains relevant [25]–[29]. On the other hand, construction of URM buildings continues, and accordingly, seismic design procedures and code regulations regarding URM construction are current topics of high importance [30]–[33].

The main purpose of the present paper is to perform a lateral strength-based seismic evaluation of a URM building seismically designed based on the theory of allowable stress. Regularization of a real URM building's geometry is firstly performed. Then, a 3D FEM model of the URM building is created in SAP2000 platform and geometrical and seismic considerations of TEC are used to achieve the design. Finally, lateral strength-based seismic evaluation of the URM building is performed in accordance with TBEC. Thereby, it is investigated to what extent the seismic performance objectives of TBEC are satisfied by a typical residential URM building.

2. CONSIDERED URM BUILDING: CHARACTERISTICS AND SEISMIC DESIGN

2.1. Material Properties and Geometric Considerations

An architectural design of a two-story residential URM building with a story height of 2.7 m is achieved. Thicknesses of load-bearing masonry walls are taken to be 200 mm, which is the minimum value imposed by Turkish Earthquake Code [1]. The walls are composed of clay brick units with dimensions of 190 mm × 290 mm × 135 mm and a weight per unit of volume of 7 kN/m^3. Reinforced concrete (RC) slab of 100 mm thickness is used. A bond beam with a height of 200 mm is integrated on each load-bearing masonry wall. The uniaxial compressive strength of concrete used in slabs and bond beams is 25 MPa. The plan view of the URM building with a total area of 95.39 m^2 is shown in Figure 1.

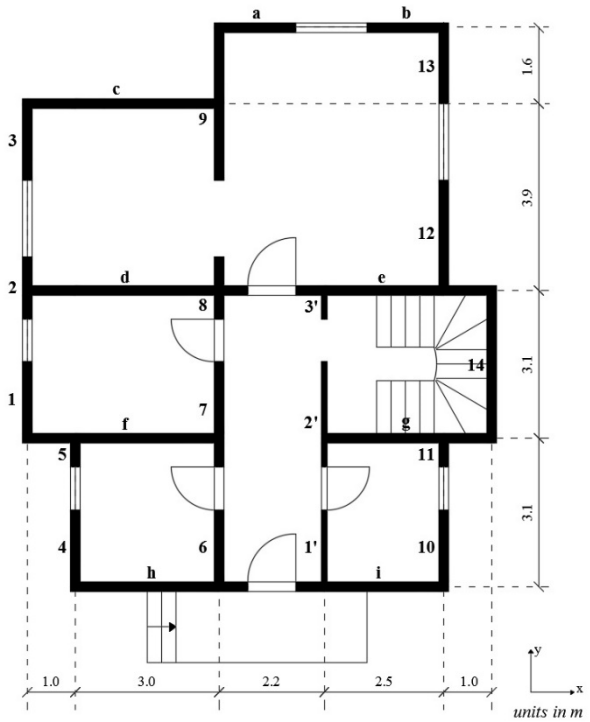

Figure 1. Plan view of URM building

Geometrical considerations of Turkish Earthquake Code are used to achieve the design. The ratio of the total length of load-bearing walls (l_d) to the floor area is computed to be 0.32 m/m^2 in x-direction and 0.25 m/m^2 in y-direction. This ratio shall not be less than 0.2I m/m^2 in two orthogonal directions. The building importance factor (I) depending on type of occupancy is 1 (i.e., I = 1). The unsupported length of load-bearing wall between the axes of load-bearing

walls in the direction perpendicular to itself is taken to be 5.5 m, which is the maximum value that can be considered for URM buildings located in seismic zone 1. The length of the solid wall parts at the corners of the building is employed to be greater than 1.5 m. In addition, this value is taken at least 0.5 m for interior walls. The length of solid walls between door and window openings, which cannot exceed 3 m and 40% of the wall length, is considered to be at least 1 m. All geometrical design criteria taken into consideration for the design of URM building are summarized in Figure 2.

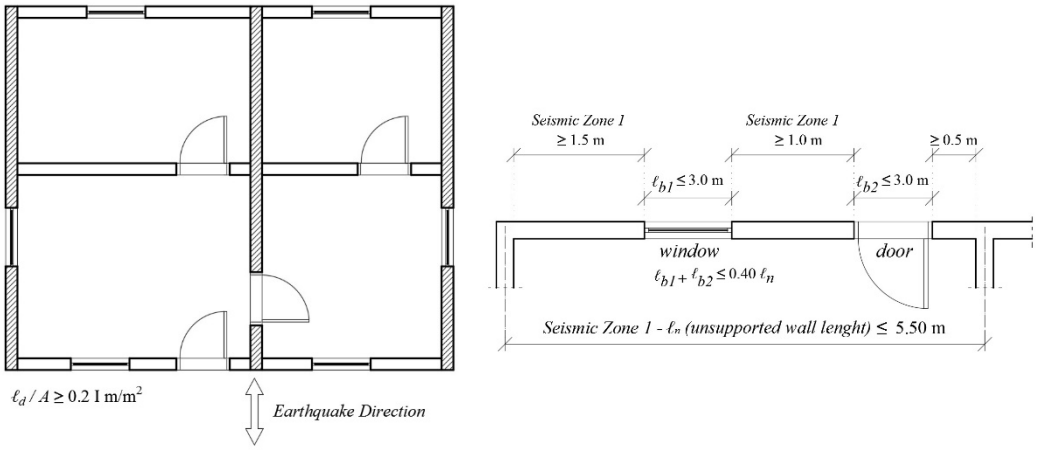

Figure 2. a) Solid wall lengths *b) Unsupported wall lengths and openings*

2.2. Seismic Design

A very detailed three-dimensional FEM model of the building is created in SAP2000 platform [34]. A modeling technique of plane finite elements is implemented to simulate masonry brick walls. Accordingly, brick masonry walls are discretized with square finite elements of 100 mm × 10 mm. Masonry elastic modulus is related to masonry compressive strength (i.e., f_{me} = 3.5 MPa), and taken to be E_{me} = 2625 MPa, whereas the expected shear modulus of masonry is employed as 0.4 times the elastic modulus. The 3D finite element model of the building is shown in Figure 3.

Having completed the analytical model, the free vibration properties of the URM building are calculated as a result of an eigenvalue analysis conducted in SAP2000 platform. Seismic masses are calculated as the combination of dead loads (i.e., elements self-weight), and 30% of live loads, which are assumed uniformly distributed on floors and taken equal to 2 kN/m^2. Accordingly, the total seismic mass is computed to be 118. 84 tons. Elastic fundamental period of vibration of the URM building is obtained to be 0.064 and 0.058 s in *x*- and *y*- directions, respectively. It is quite clear that the URM building has short vibration periods, which means that it receives elastic spectral forces specified in the acceleration amplification region of the design spectrum.

The studied URM building is designed according to 5% damped horizontal elastic acceleration response spectrum of the 2007 version of Turkish Earthquake Code representing the design basis ground motion with a reference exceedance probability of 10% in 50 years. The peak ground acceleration is 0.4*g*, where *g* is the gravitational acceleration. The considered URM building is of ordinary importance and it is assumed to be on soil with an average shear-wave velocity in the upper 30 m of the soil profile of $360 < V_{S30} \leq 760$ m/s. A response reduction factor of 2 (i.e., $R_a(T_1) = 2$) is employed to account for the reduced design spectrum.

Shear stresses developed in masonry walls subjected to design basis earthquake loading are computed as a result of finite element analyses conducted in SAP2000 platform. The seismic design of the considered URM building is achieved by satisfying the allowable shear stress criteria of Turkish Earthquake Code given in Eq. (1):

$$\tau \leq \tau_0 + \mu \cdot \sigma \quad (1)$$

where τ is the computed shear stress in a masonry wall, τ_0 is the allowable cracking stress of a masonry wall, μ is the coefficient of friction which can be taken as 0.5 according to Turkish Earthquake Code, and σ is the vertical compression stress developed in a masonry wall. The allowable cracking stress of a masonry wall is taken to be 0.25 MPa.

Considering the vertical compression stress developed in masonry walls, the allowable shear stress is computed as 0.35 MPa. The maximum shear stresses in the first story are obtained to be smaller than 0.35 MPa in *x*- and *y*-directions.

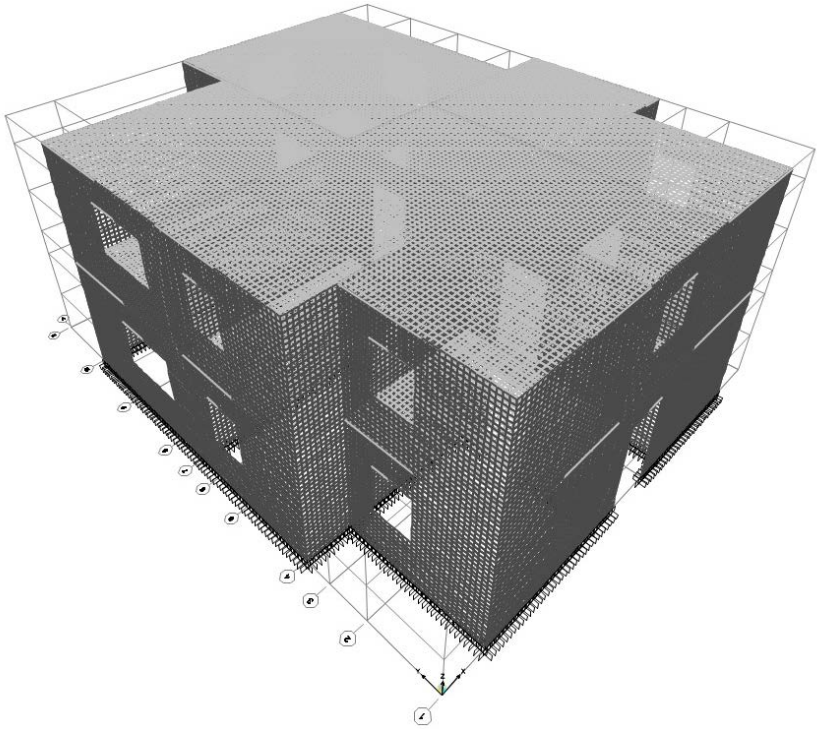

Figure 3. Finite element model of URM building

3. LATERAL STRENGTH-BASED SEISMIC EVALUATION

Lateral strength-based seismic evaluation of URM building is performed in accordance with TBEC [2]. The total design base shear forces in two orthogonal horizontal directions are computed from the elastic acceleration response spectrum of TBEC. The peak ground acceleration (PGA) of the considered earthquake is 0.708 g, where g is the gravitational acceleration, and the peak ground velocity (PGV) is 56.19 cm/s. The mapped short-period spectral response acceleration parameter (S_S) and the mapped spectral response acceleration parameter at a period of 1 s (S_1) are 1.735 and 0.469, respectively. Accordingly, spectral response acceleration parameters at short period (S_{DS}) and 1 s period (S_{D1}) are calculated to be 2.082 and 0.704, respectively. Corner periods for the employed horizontal elastic acceleration design spectrum are computed as T_A = 0.068 s and T_B = 0.338 s.

The vertical earthquake load effect is approximated by

$$E_v = (2/3)S_{DS} \cdot G \tag{2}$$

where S_{DS} is the design spectral response acceleration parameter at short period and G is the effect of dead load. The URM building is analyzed under combined earthquake and gravity loads using several combinations of factored loads and the resultant design shear forces are obtained.

The seismic performance evaluation of URM buildings according to TBEC is based on a comparison of lateral shear force capacity (V_{Rd}) of load-bearing walls with corresponding design shear force (V_{Ed}) in two orthogonal directions. The lateral shear force capacity of a load-bearing wall is considered the smallest value obtained from Eq. (3):

$$V_{Rd} = 0.5 f_{vk} \cdot t \cdot l_c \tag{3a}$$

$$V_{Rd} = l \cdot t \cdot \frac{0.75 f_{vko}}{b} \sqrt{1 + \frac{N_{Ed}}{0.75 l \cdot t \cdot f_{vko}}} \tag{3b}$$

where t is the wall thickness, l_c is the wall-length in compression, l is the wall length, b is the ratio of wall height to wall length and shall not be taken less than 1 and greater than 1.5 for use in Eq. (3b), f_{vko} is the initial characteristic shear strength of masonry wall, and N_{ed} is the design vertical force. The characteristic shear strength of masonry walls (f_{vk}) can be obtained through Eq. (4) considering the average vertical compression stress (σ_d) and shall not exceed 10% of masonry unit compressive strength (f_b):

$$f_{vk} = f_{vko} + 0.4\sigma_d \leq 0.10 f_b \quad (4)$$

4. RESULTS AND DISCUSSION

Maximum shear forces developed in load-bearing masonry walls, as well as the corresponding lateral shear strength of load-bearing masonry walls, are listed in Table 1, where wall IDs of lower case letters and numbers stand for load-bearing masonry walls oriented in *x*- and *y*-directions has shown in Figure 1. It can be seen from the data in Table 1 that the shear force capacities of three masonry walls (wall ID c, d, and e) oriented in *x*-direction on the first floor are exceeded. Moreover, the shear force capacities of three masonry walls (wall ID 7, 9, and 14) oriented in *y*-direction on the first floor are also exceeded. However, design earthquake-induced shear forces acting on second-floor masonry walls are computed to be smaller than the shear force capacities of the corresponding walls.

Table 2. Comparison of shear force demands with capacity related limits

		Developed shear forces (kN)		Shear force capacities (kN)	
	Wall ID	1st floor	2nd floor	1st floor	2nd floor
x- direction	a	40.08	24.92	56	53.77
	b	38.65	19.88	56	54.59
	c	161.63	118.16	140	140
	d	162.46	121.55	161	161
	e	146.66	118.20	143	143.5
	f	120.60	86.85	140	140
	g	98.40	67.37	122.5	122.5
	h	101.57	69.28	126	126
	i	85.44	53.65	108.5	108.5
y- direction	1	46.36	28.15	56.00	55.02
	2	25.31	13.16	45.50	43.55
	3	41.62	19.43	56.00	56.00
	4	43.53	23.24	56.00	55.20
	5	11.21	11.62	20.69	18.98
	6	46.10	32.80	56.00	56.00
	7	79.22	49.49	77.00	77.00
	8	32.08	29.85	45.50	39.76
	9	137.45	84.46	112.00	112.00
	1'	25.02	18.73	51.12	48.28
	2'	38.86	24.87	77.00	77.00
	3'	5.60	8.82	21.00	20.23
	10	42.90	24.52	56.00	55.75
	11	11.29	12.69	20.56	18.58
	12	80.18	54.11	80.50	80.50
	13	44.05	19.68	56.00	54.33
	14	135.92	106.73	108.50	108.50

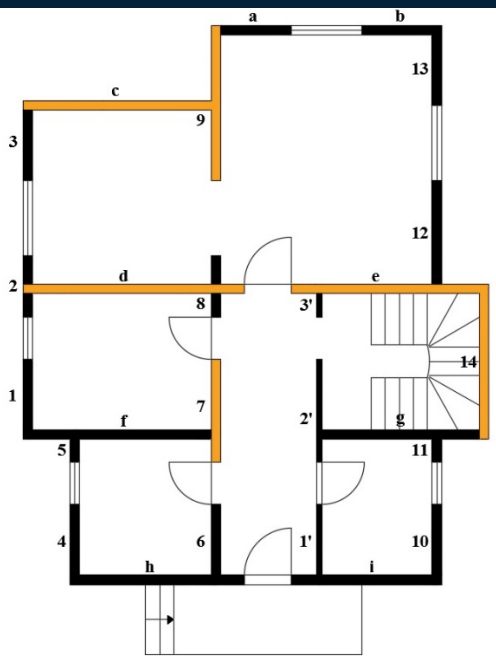

Figure 4. Damaged masonry walls (in orange)

Load-bearing masonry walls of which shear force capacities are exceeded are shown in orange in Figure 4. Relatively high shear forces are developed in these masonry walls due to their excessive rigidities. The contribution of these masonry walls to story shear force is computed to be 49.27% and 41.64%, respectively in *x*- and *y*- directions. These ratios are greater than 40%, the limiting value of TBEC. It is apparent from this result that the considered URM building does not satisfy the collapse prevention performance objective of TBEC.

On the other hand, shear force demands imposed on masonry walls “d” and “e” are slightly greater than their capacities (i.e., the demand/capacity ratio of these walls is 1.009 and 1.026, respectively). The same finding is observed for wall “7”, where the shear force demand/capacity ratio is computed to be 1.029. It is quite clear that both earthquake demand and capacity of a masonry wall are inherently probabilistic concepts. If the demand/capacity ratio of the aforementioned masonry walls were slightly below 1, the same building would satisfy the damage control performance level of TBEC.

5. SUMMARY AND CONCLUSIONS

The seismic performance of a three-dimensional URM building which is seismically based on the theory of allowable stress is evaluated comprehensively by considering the lateral strength-based criteria of TBEC. The analyses are conducted based on the finite element model of the building. The following conclusions can be drawn from the presented study:

- Although the considered URM building is seismically designed according to allowable stress criteria of the 2007 version of Turkish Earthquake Code, it does not satisfy the collapse prevention performance objective of TBEC.
- Remarkable high shear forces are developed in long masonry walls. These walls cannot sustain the high shear forces due to their relatively low capacities of shear force.
- First-story load-bearing masonry walls are found to be more vulnerable to earthquake loading.
- Both seismic demand and capacity are probabilistic concepts. Accordingly, it is quite questionable to assign deterministic values limiting seismic performance levels without considering the scattering, as implemented in TBEC.

REFERENCES

[1]. *Turkish Earthquake Code (TEC)*, Ministry of Public Works and Settlement, Ankara, Turkey, 2007, (in Turkish).
[2]. *Turkey Building Earthquake Code (TBEC)*, Ministry of Public Works and Settlement, Ankara, Turkey, 2018, (in Turkish).
[3]. R. Marques, and P.B. Lourenco, "Possibilities and comparison of structural component models for the seismic assessment of modern unreinforced masonry buildings", *Computers and Structures*, vol. 89, pp. 2079–2091, 2011.
[4]. A.H. Akhaveissy, "Finite element nonlinear analysis of high-rise unreinforced masonry building", *Latin American Journal of Solids and Structures*, vol. 9, pp. 1–22, 2012.
[5]. I. Caliò, M. Marletta, and B. Pantò, "A new discrete element model for the evaluation of the seismic behavior of unreinforced masonry buildings", *Engineering Structures*, vol. 40, pp. 327–338, 2012.
[6]. Y. Nakamura, H. Derakhshan, A.H. Sheikh, J.M. Ingham, and M.C. Griffith, "Equivalent frame modelling of an unreinforced masonry building with flexible diaphragms – A case study", *Bulletin of the New Zealand Society for Earthquake Engineering*, vol. 49, pp. 234–244, 2016.
[7]. R. Siano, G. Camata, V. Sepe, E. Spacone, P. Roca, and L. Pelà, "Numerical validation of equivalent-frame models for URM walls", in *Proc. VII European Congress on Computational Methods in Applied Sciences and Engineering*, 2016.
[8]. E. Quagliarini, G. Maracchini, and F. Clementi, "Uses and limits of the Equivalent Frame Model on existing unreinforced masonry buildings for assessing their seismic risk: A review", *Journal of Building Engineering*, vol. 10, pp. 166–182, 2017.
[9]. A. Shabani, M. Kioumarsi, and M. Zucconi, "State of the art of simplified analytical methods for seismic vulnerability assessment of unreinforced masonry buildings", *Engineering Structures*, vol. 239, 112280, 2021.
[10]. S. Cattari, B. Calderoni, I. Caliò, G. Camata, S. Miranda, G. Magenes, G. Milani, and A. Saetta, "Nonlinear modeling of the seismic response of masonry structures: critical review and open issues towards engineering practice", *Bulletin of Earthquake Engineering*, vol. 20, pp. 1939–1997, 2022.
[11]. M. A. ElGawady, P. Lestuzzi, and M. Badoux, "In-plane seismic response of URM walls upgraded with FRP", *Journal of Composites for Construction*, vol. 9, pp. 524–535, 2005.
[12]. T. Yi, F.L. Moon, R.T. Leon, and L.F. Kahn, "Analyses of a two-story unreinforced masonry building", *Journal of Structural Engineering*, vol. 132, pp. 653–662, 2006.
[13]. Q. Ali, and A. Naeem, "Seismic resistance evaluation of unreinforced masonry buildings", *Journal of Earthquake Engineering*, vol. 11, pp. 133–146, 2007.
[14]. G. M. Verderame, P. Ricci, and M. D. Domenico, "Experimental vs. theoretical out-of-plane seismic response of URM infill walls in RC frames", *Structural Engineering and Mechanics*, vol. 69, pp. 677–691, 2019.
[15]. H. Sucuoglu, and A. Erberik, "Performance evaluation of a three-storey unreinforced masonry building during the 1992 Erzincan Earthquake", *Earthquake Engineering and Structural Dynamics*, vol. 26, pp. 319–336, 1997.
[16]. D.P. Abrams, "Performance-based engineering concepts for unreinforced masonry building structures", *Progress in Structural Engineering and Materials*, vol. 3, 48–56, 2001.
[17]. J. Ingham, and M. Griffith, "Performance of unreinforced masonry buildings during the 2010 Darfield (Christchurch, Nz) Earthquake", *Australian Journal of Structural Engineering*, vol. 11, pp. 207–224, 2010.
[18]. J.K. Bothara, R.P. Dhakal, and J.B. Mander "Seismic performance of an unreinforced masonry building: An experimental investigation", *Earthquake Engineering and Structural Dynamics*, vol. 39, pp. 45–68, 2010.
[19]. S.S. Khadka, "Seismic performance of traditional unreinforced masonry building in Nepal", *Kathmandu University Journal of Science, Engineering and Technology*, vol. 9, pp. 15–28, 2013.
[20]. N. Shkodrani, H. Bilgin, and M. Hysenlliu, "Influence of interventions on the seismic performance of URM buildings designed according to pre-modern codes", *Research on Engineering Structures and Materials*, vol. 7, pp. 315–330, 2021.
[21]. L.F. Restrepo-Velez, and G. Magenes, "Simplified procedure for the seismic risk assessment of unreinforced masonry buildings", in *Proc. 13th World Conference on Earthquake Engineering*, 2004, Paper No. 2561.
[22]. A.J. Kappos, G. Panagopoulos, C. Panagiotopoulos, G. Penelis, "A hybrid method for the vulnerability assessment of R/C and URM buildings", *Bulletin of Earthquake Engineering*, vol. 4, pp. 391–413, 2006.
[23]. A.P. Russell, and J.M. Ingham, "Prevalence of New Zealand's unreinforced masonry buildings", *Bulletin of the New Zealand Society for Earthquake Engineering*, vol. 43, pp. 182–201, 2010.
[24]. A.B. Acevedo, J.D. Jaramillo, C. Yepes, V. Silva, F.A. Osorio, and M. Villar, "Evaluation of the seismic risk of the unreinforced masonry building stock in Antioquia, Colombia", *Natural Hazards*, vol. 86, pp. S31–S54, 2017.
[25]. S.W. Chuang, and Y. Zhuge, "Seismic retrofitting of unreinforced masonry buildings – A literature review", *Australian Journal of Structural Engineering*, vol. 6, pp. 25–36, 2005.
[26]. S. Frumento, S. Giovinazzi, S. Lagomarsino, and S. Podestà, "Seismic retrofitting of unreinforced masonry buildings in Italy", in *Proc. 2006 NZSEE Conference*, 2006, Paper 48.
[27]. G. Z. Ahari, and K. Yamaguchi, "A proposal of the most suitable retrofitting methods for URM structures in Iran – An extensive review of recent techniques", *Journal of Habitat Engineering*, vol. 22, pp. 105–114, 2010.
[28]. S. Bhattacharya, S. Nayak, and S. C. Dutta, "A critical review of retrofitting methods for unreinforced masonry structures", *International Journal of Disaster Risk Reduction*, vol. 7, pp. 51–67, 2014.
[29]. F. Yavartanoo, and T. H.-K. Kang, "Retrofitting of unreinforced masonry structures and considerations for heritage-sensitive constructions", *Journal of Building Engineering*, vol. 49, 103993, 2022.
[30]. M.A. Erberik, A. Aldemir, and B.O. Ay, "A critique on the Turkish earthquake code regulations regarding masonry construction", in *Proc. 8th International Seminar on Structural Masonry*, 2008.
[31]. C. F. Manzini, G. Magenes, A. Penna, F. Porto, D. Camilletti, S. Cattari, and S. Lagomarsino, "Masonry Italian code-conforming buildings. Part 1: Case studies and design methods", *Journal of Earthquake Engineering*, vol. 22, pp. 54–73, 2018.

[32]. S. Marino, S. Cattari, and S. Lagomarsino, "Use of nonlinear static procedures for irregular URM buildings in literature and codes", in. *Proc. 16th European Conference on Earthquake Engineering*, 2018.

[33]. P. Morandi, C.F. Manzini, and G. Magenes, "Application of seismic design procedures on three modern URM buildings struck by the 2012 Emilia earthquakes: Inconsistencies and improvement proposals in the European codes", *Bulletin of Earthquake Engineering*, vol. 18, pp. 547–580, 2020.

[34]. *SAP2000 Ultimate Integrated Solution for Structural Analysis and Design*, Version 20.2.0, Computers and Structures Inc. (CSI), Berkeley, California, USA, 2018.

ICENS 8TH INTERNATIONAL CONFERENCE ON ENGINEERING AND NATURAL SCIENCE
May 18-22 2022 Istanbul (Hybrid Event)

The Forecast of Value of Lost Load in Slovenia

***Jerneja Bogovič*[1]**

Abstract

In modern society, we are increasingly dependent on electricity, which makes interruptions in supply affect us even more and also causes both direct and indirect costs. Various indexes are available to evaluate the costs associated with interruptions in supply. Recently, the Value of Lost Load (VOLL) has been the most commonly used index to evaluate costs. Moreover, a determination of this index is mandatory in the EU and ENTSO-E countries, as a measure of the Reliability Standard. Since the determination of the VOLL based on surveys is time-consuming and estimates based on macroeconomic indicators do not provide realistic values, a regression method with the gross domestic product (GDP) as the impact factor is used to forecast the value of the VOLL for Slovenia until the year 2030. The estimated value of the VOLL for Slovenia in 2022 is 10.0€/kWh, which is in line with the value of 10.6€/kWh used to measure the Reliability Standard in Slovenian electric power system. Furthermore, the obtained results are compared with the results for Italy, which has carried out a survey-based analysis in 2021 and has a GDP in 2021 slightly higher than projected for Slovenia in 2030. Based on the regression method, the value of the VOLL for Slovenia for 2030 is estimated at 26.0€/kWh, while the value of the VOLL for Italy in 2021 based on survey is 28.4€/kWh. The results show that the application of the regression method to predict the value of the VOLL using the GDP as impact parameter is reasonable and appropriate.

Keywords: Gross domestic product (GDP), Regression, Reliability Standard, Slovenian power system, Value of lost load (VOLL)

1. INTRODUCTION

In modern society, we are increasingly dependent on the use of electricity, so the continuity of power supply is essential for the functioning of the society. However, in certain, albeit very rare cases, the power supply is interrupted.

Each interruption of the power supply can incur costs for the customer. Their size is affected by the different nature and diversity of the consequences of power supply interruption. For household customers, costs can be reflected in the form of:

- lost income,
- deterioration of living quality,
- costs due to repair and wear of appliances,
- replacement of unsupplied electricity, and
- in the case of prolonged outages, also as food destruction.

However, in the industry sector the costs of unsupplied electricity are incurred due to:

- additional material consumption,
- repair of fixed assets,
- restart the process,

[1] *Corresponding author: Jerneja Bogovič, University of Ljubljana, Faculty of Electrical Engineering, Laboratory of Power Systems, 1000 Ljubljana, Slovenia. jerneja.bogovic@fe.uni-lj.si*

- replacement of unsupplied electricity
- costs due to delays, and
- loss of sales.

A special group of costs is the costs of civil disobedience and looting during prolonged downtime and failures of safety devices in industrial plants, which can lead to mandatory evacuation from all facilities in the area [1].

The literature [2] describes several methods for calculating the value of unsupplied electricity, which is defined as the monetary value of costs, normalized to unsupplied electricity. Methods can generally be divided into three groups:

- **Survey of customers** is the most common method for evaluating cost because of unsupplied electricity. Based on the questionnaire, the respondent assesses the damage or monetary loss suffered in case of interruption of the power supply. The disadvantage of the method is that the customer either overestimates or underestimates the costs associated with interruption of the power supply. In addition to the damage survey, a survey, in which respondents are asked about the willingness to pay so that he will not suffer a supply interruption, or to evaluate the compensation in the case of a supply interruption, can also be used.
- **Specific outage studies** are most commonly used when actual power outages occur. This method gives the best estimate of the damage, but is not useful in cases where there has been no power failure in the past.
- **Indirect analytical assessments** define the value of unsupplied electricity on the basis of various macroeconomic indicators. The advantage of this method is that the estimates are easy to calculate. However, its disadvantage is that they are based on limiting and sometimes unrealistic assumptions.

In addition to various methods, various indicators are also used to evaluate the value of unsupplied electricity [3], which are:

- Cost of Energy Not Supplied – *CENS*,
- Value of Lost Load – *VOLL*, and
- Interrupted Energy Assessment Rate – *IEAR*.

Although various indicators have been developed to evaluate undelivered electricity, the *VOLL* indicator is the most commonly used. The main reason for this is also Regulation (EU) 2019/943 of the European Parliament and of the Council of the European Union on the internal market for electricity [4]. The regulation determines that European Union (EU) countries must develop reliability standards based on the methodology Methodology for calculating the value of lost load, the cost of new entry and the reliability standard [5]. The methodology defines the procedure for calculating the *VOLL* indicator, which is based on the survey method. The methodology also requires that the *VOLL* indicator based on survey method must be calculated every 5 years.

However, as the values of the *VOLL* indicator changes over the years, the forecast of the *VOLL* indicator until the year 2030 using regression depending on gross domestic product (*GDP*) has been used in this paper to speed up the process of determining the *VOLL* indicator.

2. METHODOLOGY FOR FORECASTING THE VOLL INDICATOR

Generally, forecasting is the process of making predictions based on past and present data, where different qualitative and quantitative methods can be used. Qualitative forecasting techniques are subjective, based on the opinion and judgment of consumers and experts and are appropriate when past data are not available. On the other hand, quantitative forecasting techniques are used to forecast future data as a function of past data. They are appropriate to use when past numerical data is available and when it is reasonable to assume that some of the patterns in the data are expected to continue into the future. Quantitative forecasting techniques comprise different methods as time series methods, artificial intelligence methods, extrapolation and relational methods [6].

In this paper, one of the relation methods has been used. More specifically, the regression analysis has been used to predict the value of the *VOLL* indicator. Regression analysis is a statistical method used in finance, investing, and other disciplines that attempts to determine the strength and character of the relationship between

one dependent variable and a series of other impact variables. Mathematical form of connection can be linear, power, exponential, reciprocal, logarithmic, root … In practice, a linear connection (1) is most often used, also that a nonlinear regression relationship is attempted to be transformed into a linear relationship by transforming variables [7].

$$Y = \beta_1 \cdot X + \beta_2 \tag{1}$$

In the next step, theoretical assumptions about the dependence between variables are made to make a regression analysis. As statistically significant, the Cambridge Economic Policy Associates [8] study showed a trend that EU countries with a higher standard of living also have higher values of *VOLL* indicator. As one of the macroeconomic parameters, describing the standard is also *GDP*, it has been used as impact parameter for forecasting the *VOLL* indicator by regression analysis.

The next step is to calculate or estimate the parameters of the regression model, where the parameters of the model are determined by the method of least squares. The least squares method is the standard approach for determining the dependence function of an oversized system, by minimizing the sum of the squares of the deviations.

The last step is the calculation or forecast the value of the *VOLL* indicator based on the regression function determined in the previous steps.

3. THE FORECAST OF VOLL INDICATOR

To forecast the value of the *VOLL* indicator by the regression method, at first the influencing factor has been selected. As it is mentioned in the literature [8] that there is a statistical connection between the standard of living and *VOLL* indicator, we chose the macroeconomic indicator of *GDP* per capita as an influential factor. *VOLL* indicator, obtained on the basis of the survey method, was determined in years 1995, 2006 and 2016. For these years, the *VOLL* indicator as a function of *GDP* is drawn in the Figure 1.

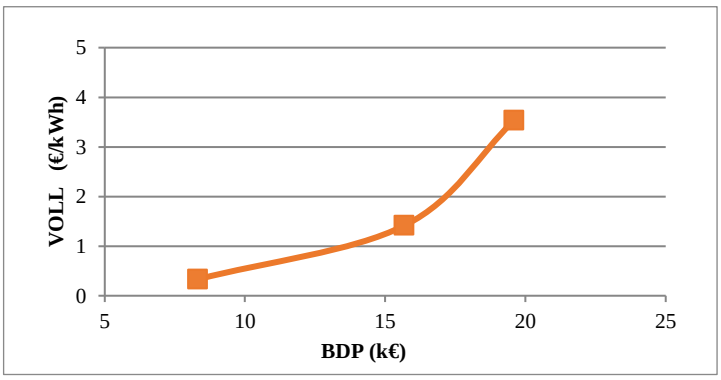

Figure 1. GDP per capita - dependent VOLL indicator

The next step in the forecast using the regression method is the selection of the regression model. Since Figure 1 shows that the most commonly used linear relationship is not the best possible relationship for this case, the transformation of the *VOLL* variable was performed. For that reason the transformation (logarithmization) of the *VOLL* indicator was performed and the result was a linear relationship between the *BDP* per capita and *VOLL* indicator (Figure 2).

The next step was determination of regression (linear) function parameters using the least squares method. The linear function that connects the *GDP* per capita and the *VOLL* indicator is given by the equation (2).

$$ln(VOLL) = 0.2085 \cdot BDP - 2.8627 \quad (2)$$

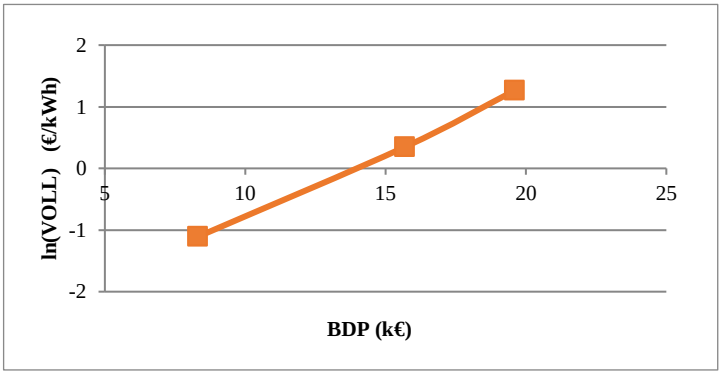

Figure 2. GDP per capita - dependent logarithmize VOLL indicator

Based on the GDP forecast until 2030 [9], the VOLL indicator for all subsequent years has been calculated and are presented in Table 1 and on Figure 3. As it can be seen from Table 1, *BDP* per capita is increasing over the coming years. Due to the linear dependence, this trend is also followed by the value of the *VOLL* indicator.

Table 3. Forecast of VOLL indicator

Year	***BDP per capita* (k€)**	**ln(*VOLL*) (€/kWh)**	***VOLL* (€/kWh)**
2022	24,772	2.3	10.0
2023	25,293	2.4	11.1
2024	25,827	2.5	12.4
2025	26,377	2.6	13.9
2026	26,942	2.8	15.7
2027	27,522	2.9	17.7
2028	28,119	3.0	20.0
2029	28,732	3.1	22.8
2030	29,362	3.3	26.0

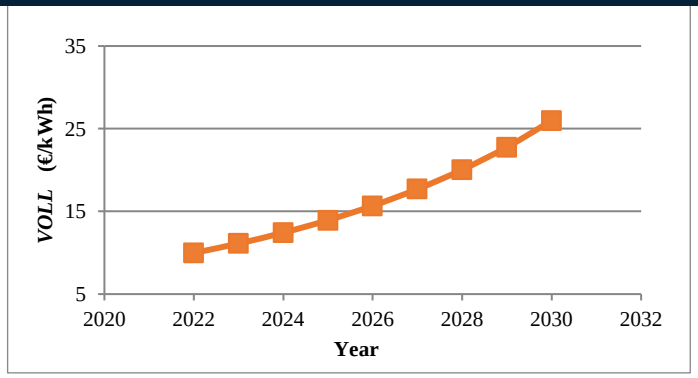

Figure 3. Forecast of VOLL indicator

At this point, the question is whether the forecast is realistic or not. The estimated value of the *VOLL* indicator for Slovenia in 2022 is 10.0 €/kWh, which is in line with the value of 10.6 €/kWh used by Slovenian transmission system operator [1].

Furthermore, the obtained results are compared with the results for Italy, which has carried out a survey-based analysis in 2021 and has a *GDP* per capita in 2021 slightly higher than projected for Slovenia in 2030. Based on the regression method, the value of the *VOLL* indicator for Slovenia for 2030 is estimated at 26.0 €/kWh, while the value of the *VOLL* indicator for Italy in 2021 based on survey is 28.4 €/kWh [10]. The results are in range of ± 10 % of estimation error, which we considered as good estimations, as not much data was available to calculate or estimate the parameters of the regression model.

CONCLUSIONS

In this paper, we predicted the value of the *VOLL* indicator using regression analysis. With regression analysis, we first developed a regression model, based on which we predicted the value of *VOLL* indicator for years from 2022 to 2030, where *BDP* per capita is used as an impact factor to forecast the value of the *VOLL* indicator.

The estimated value of the *VOLL* indicator for Slovenia in 2022 is 10.0 €/kWh, which is in line with the value of 10.6 €/kWh used by Slovenian transmission system operator. The estimated value of the *VOLL* indicator for Slovenia in 2030 has been also evaluated and the error is in range of ± 10 %.

The field of forecasting is a very sensitive topic, especially when there is not much data available. Also in our case, not much data was available, which made it impossible to perform a more detailed analysis and comparison of the final results.

ACKNOWLEDGMENT

This work was supported by a Slovenian Research Agency as a part of the research program Electric Power Systems, P2–356.

REFERENCES

[1]. F. Hočevar, J. Bogovič, K. Dragaš, and M. Pantoš, “Vrednotenje nedobavljene električne energije,” in Referati in predstavitve 14. konference slovenskih elektroenergetikov CIGRE-CIRED, 2019, pp. 1–6.
[2]. A. Shivakumar et al., “Valuing blackouts and lost leisure: Estimating electricity interruption costs for households across the European Union,” Energy Res. Soc. Sci., vol. 34, no. Supplement C, pp. 39–48, Dec. 2017.
[3]. Z. Bozic, “Customer interruption cost calculation for reliability economics: practical considerations,” in 2000 International Conference on Power System Technology Proceedings, 2000, pp. 1095-1100.
[4]. Regulation (EU) 2019/943 of the European Parliament and of the Council of 5 June 2019 on the internal market for electricity (Text with EEA relevance.), vol. 158. 2019.
[5]. Methodology for calculating the value of lost load, the cost of new entry and the reliability standard, ACER, 2020.
[6]. Forecasting, Wikipedia, 2022.
[7]. J. Bogovič, “Vrednost nedobavljene električne energije v Sloveniji,” Elektrotehniški vestnik, vol. 88, no. 5, pp. 236–240, 2021.
[8]. Study on the value of lost load of electricity supply in Europe - ACER, Cambridge Economic Policy Associates, 2018.

[9]. B. Tavčar, I. Zakotnik, I. Strmšnik, and T. Kraigher, Scenariji gospodarskega razvoja Slovenije do leta 2030, Urad RS za makroekonomske analize in razvoj, Ljubljana, 2007.
[10]. Proposta in merito allo standard di adeguatezza del sistema elettrico Italiano, Terna, 2020.

BIOGRAPHY

Jerneja Bogovič received B.Sc. and Ph.D. degrees in electrical engineering from the Faculty of Electrical Engineering, University of Ljubljana, Ljubljana, Slovenia, in 2011 and 2017, respectively. She is currently an assistant with the Faculty of Electrical Engineering, University of Ljubljana. Her areas of interest include power-system modeling and analysis and FACTS devices.

ICENS 8TH INTERNATIONAL CONFERENCE ON ENGINEERING AND NATURAL SCIENCE
May 18-22 2022 Istanbul (Hybrid Event)

Review of the reliability standards in EU electric power system

***Jerneja Bogovič*[1]**

Abstract

Security of supply is one of the main objectives of a comprehensive package of EU legislative acts called Clean Energy for All Europeans. Through these legislative acts, the EU aims to accelerate the deployment of clean technologies, increase market competitiveness and energy efficiency, outline the design of the electricity market and security of supply, and create new rules for the governance of the Energy Union, making the European electricity market more interconnected, flexible and consumer-oriented.

One of the main objectives is to determine the most efficient and effective way to ensure appropriate adequacy of generation units in the EU. In October 2020, European Union Agency for the Cooperation of Energy Regulators (ACER) presented the Methodology for calculating the value of lost load, the cost of new entry, and the reliability standard, which specifies the security of supply indexes and define the methodology for their calculation.

Therefore, each EU Member State has to determine the value of lost load (VOLL), the cost of new entry (CONE) for different candidate technologies that are able to provide resource adequacy benefits (generation, storage and demand side response), and the reliability standard that consists of expected energy not served and loss of load expectation.

The paper provides an overview of the methodology and results for countries that have already defined reliability standards according to the new methodology.

Keywords: Cost of new entry for generation or demand response (CONE), Expected energy not served (EENS), Loss of load expectation (LOLE), Value of lost load (VOLL)

1. INTRODUCTION

The primary task of a transmission system operator is the power transmission, where the reliability of the power system is important. The most important factor in reliability is the continuity of supply of the final customers. Security of supply is also one of the objectives of the publication of a comprehensive package of legislative acts called Clean Energy for All Europeans [1]. Article 25 of the regulation provides that Member States have to draw up a reliability standard based on the methodology referred to in Article 23(6).

The reliability standard shall set out in a transparent manner the required level of security of supply to the Member State determined as the most efficient and effective way to ensure appropriate adequacy of generation units in the EU. The reliability standard is calculated using at least the value of the lost load (*VOLL*) and the cost of new entry (*CONE*) and is expressed as expected energy not served (*EENS*) and loss of load expectation (*LOLE*). Thus, the *LOLE* indicator reflects the economic optimization between the cost of new entry (*CONE*) and the marginal reduction in expected electricity not served (*EENS*), expressed as the product of *LOLE* × *VOLL*.

In October 2020, European Union Agency for the Cooperation of Energy Regulators (ACER) presented the document Methodology for calculating the value of lost load, the cost of new entry, and the reliability standard, which specifies the security of supply indexes and define the methodology for their calculation [2]. Under Regulation (EU) 2019/943, Member States have started activities in the field of defining the reliability standard.

[1] *Corresponding author: Jerneja Bogovič, University of Ljubljana, Faculty of Electrical Engineering, Laboratory of Power Systems, 1000 Ljubljana, Slovenia. jerneja.bogovic@fe.uni-lj.si*

The activities were started mainly by countries that already had reliability standards defined before the adoption of the regulation.

Therefore, the methodology for calculating the reliability standards will first be presented and followed by an overview of the reliability standards per Member State.

2. METHODOLOGY FOR CALCULATING THE RELIABILITY STANDARDS

Methodology for calculating the value of lost load, the cost of new entry, and the reliability standard [2], describes how to calculate:

- the *VOLL*,
- the *CONE* and
- the reliability standard.

General rules for determination of all three indicators are:

- The entity calculating the *VOLL*, *CONE* and reliability standard shall update the calculation at least every five years, or earlier, where the entity observes a significant change.
- The entity has to ensure that the procedure is based on transparent, objective and verifiable data, the entity shall fulfil the transparency requirements, publishing at least the basic information, that the calculation of the *VOLL*, *CONE* and reliability standard can be repeatable.

However, the rules relating to the determination of each indicator are presented in the following subsections.

2.1. VOLL

In [2], there are specified several rules that must be taken into consideration for determination of *VOLL*. The determination of *VOLL* must be set from the maximum price that consumers are willing to pay to avoid an interruption of electricity supply, obtained from surveys. The structure of the survey is also predefined in the [2]. Based on the answers, the each sectoral *VOLL* for different outages (duration, period of occurrence, pre-notification period) shall be defined. The next step in determination of *VOLL* is a single *VOLL* calculation that will be used in the determination of reliability standard (1).

$$VOLL = \sum_{type} VOLL_{sect,type} \cdot \frac{EENS_{sect,type}}{EENS} \quad (1)$$

where $VOLL_{sect,type}$ is *VOLL* for different sectorial and outages, $EENS_{sect,type}$ is expected electricity not served for different sectorial and outages and *EENS* is expected electricity not served for entire country.

2.2. CONE

In [2], there are also specified several rules that must be taken into consideration for determination of *CONE*. The following steps shall be performed in order to calculate the *CONE*:

- Review and select candidate technologies that can be considered as reference technologies and estimate the potential for additional capacity resource.
- Define the detailed technical characteristics of the reference technologies.
- Estimate capital costs and annual fixed costs for each reference technology.
- Determine an appropriate *WACC* for each reference technology as in (2).
- Compute $CONE_{fixed}$ for each reference technology (3).
- Determine $CONE_{var}$ for each reference technology.

$$WACC = \frac{1+\left[CoE\cdot\frac{1-g}{1-t}+CoD\cdot g\right]}{1+i} - 1 \quad (2)$$

where *CoE* represents the cost of equity, *CoD* represents the cost of debt, *g* represents the gearing, *t* corresponds to tax rate and *i* represents the long-term inflation rate of the Euro zone.

$$CONE_{fixed} = \frac{\frac{WACC\cdot(1+WACC)^{X+Y}}{(1+WACC)^{Y}-1}\cdot\left[\sum_{I=1}^{X}\frac{CC(i)}{(1+WACC)^{i}}+\sum_{I=X+1}^{X+Y}\frac{AFC(i)}{(1+WACC)^{i}}+\right]}{K_d} \quad (3)$$

where *i* represents each year over the construction period and economic lifetime, *X* is the construction period (in years), *Y* is the economic lifetime (in years), *CC*(*i*) is the best estimate of the capital costs incurring each year of the construction period, *AFC*(*i*) is the best estimate of the annual fixed costs incurring each year during the economic lifetime, *WACC* is the best estimate of *WACC* and K_d is the de-rating capacity factor of the reference technology.

For each reference new entry, which has a variable cost ($CONE_{var}$) lower than the single *VOLL* the entity shall compute a *LOLE* threshold (4).

$$LOLE_{RT} = \frac{CONE_{fixed}}{VOLL - CONE_{var}} \quad (4)$$

2.3. Reliability standard

The entity shall calculate a *LOLE* target for the reliability standard, based on the *LOLE* thresholds. The *LOLE* threshold reflects an economic optimization between the marginal cost of a new capacity resource (*CONE*) and the marginal reduction of *EENS* (*LOLE* × *VOLL*). The optimum is reached when these two quantities are equal.

The *LOLE* target for reliability standard shall be the minimum (best estimate) *LOLE* threshold which fulfils the minimum capacity need for reliability standard. A minimum capacity need for RS shall be defined based on the results of the latest available national, regional or European resource adequacy assessments (e.g. based on the relation between the observed number of hours with *ENS* and the capacity margins of the electric system). The minimum capacity need for reliability standard shall be lower than (or equal to) the maximum hourly *ENS* observed during the latest European, regional or national resource adequacy assessment [2].

There is no unambiguously defined formula for the calculation of *EENS* in [2].

3. VALUES OF VOLL, CONE AND RELIABILITY STANDARD IN EU

Several countries in EU have already prepared the calculations of *VOLL*, *CONE* in reliability based on previously described rules. These countries are Estonia, Finland, Italy and Sweden. All the countries have determined *VOLL*, *CONE* and reliability standard.

3.1. Estonia

The final report [3] provides an analysis of the *LOLE* value in the case of a gas power plant (OCGT). The value of *VOLL* is estimated at 6,500 €/MWh, 7,300 €/MWh and 8,500 €/MWh, $CONE_{fixed}$ for OCGT at 51,000 €/MW, 63,000 €/MW and 78,000 €/MW. Based on the calculations, the value of the *LOLE* is in ranges between 6 hours/year and 12 hours/year, which exceeds the standard of 3 hours/year, so in May 2021 they changed the value of the standard to 9 hours/year. Furthermore, the study also estimated the *EENS* value between 0.053% and 0.087%.

3.2. Finland

Based on the ACER methodology, the value of the *VOLL* for Finland was estimated at 8,000 €/MWh [4]. The calculation of the $CONE_{fixed}$ for various reference technologies is presented, as demand side response (DSR), OCGT, nuclear power plants (NPP), battery storage (BESS), wind power plant (WPP) and solar power plant (SPP). The data are presented in Table 1.

Table 4. $CONE_{fixed}$ for various reference technologies

Technology	$CONE_{fixed}$ (€/MW)
DSR	20,000
OCGT	60,000
NPP	537,000
BESS	570,000
WPP	1,583,000
SPP	5,128,000

Based on the data on the *VOLL* and $CONE_{fixed}$, the calculated value of the *LOLE* for determining the reliability standard is defined as 3 hours/year, and the value of the *EENS* as 1,800 MWh per year.

3.3. Italy

In early June, Terna published the study Proposta in merito allo standard di adeguatezza del sistema elettrico italiano [5], in which the calculation for *VOLL*, $CONE_{fixed}$ and *LOLE* was made according to the ACER methodology. Based on the questionnaire, they determined the value of *VOLL*, which amounts to 28,400 €/MWh. The $CONE_{fixed}$ has been defined for different technologies, which are OCGT, combined cycle gas turbine (CCGT), BESS, pumped storage hydropower (PSH), WPP and SPP. The data about $CONE_{fixed}$ are presented in Table 2.

Table 5. $CONE_{fixed}$ for various reference technologies

Technology	$CONE_{fixed}$ (€/MW)
OCGT	55,000
CCGT	71,000
BESS	141,000
PSH	200,000
WPP	380,000
SPP	500,000

Based on the calculations, they conclude that the value of *LOLE* according to the ACER methodology is between 2 and 2.1 hours/year and is lower than the value determined by the state.

3.4. Sweden

In May 2021, the Energimarknadsinspektionen (Ei) produced a report Ei:s forslag till tillforlitlighetsnorm for Sverige [6], in which, according to the ACER methodology, *VOLL* is calculated as 7,869 €/MWh and also $CONE_{fixed}$ for different technologies is specified. The data about $CONE_{fixed}$ are presented in Table 3.

Table 6. $CONE_{fixed}$ for various reference technologies

Technology	$CONE_{fixed}$ (€/MW)
DSR	3,400
OCGT	19,500
CCGT	62,700
BESS	104,900
PSH	200,000
WPP	1,100,000

Based on the calculations, a value of 0.99 hours/year was set for the *LOLE* as the limit value of the reliability standard, thus covering the highest value of production unit failures from simulations.

CONCLUSION

In the paper, a review of the new reliability standard in EU is made. Despite the fact that the new standard has been in force for quite some time, many countries still have not made a calculation according to the new methodology or have not yet made it public. From EU countries, only 4 have made the calculations, which represents 15% of all countries. The main reason for this is attributed to the publication of ERAA results. Based on the ERAA results, just a few countries have a problem with resource adequacy [7].

ACKNOWLEDGMENT

This work was supported by a Slovenian Research Agency as a part of the research program Electric Power Systems, P2–356.

REFERENCES

[1]. Regulation (EU) 2019/943 of the European Parliament and of the Council of 5 June 2019 on the internal market for electricity (Text with EEA relevance.), vol. 158. 2019.
[2]. Methodology for calculating the value of lost load, the cost of new entry and the reliability standard, ACER, 2020.
[3]. Adequacy Standard for Estonia, Elering, 2020.
[4]. Energiaviraston ehdotus asetuksen (EU) 2019/943 mukaiseksi luotettavuusstandardiksi, Energiaviraston, 2022.
[5]. Proposta in merito allo standard di adeguatezza del sistema elettrico italiano, Terna, 2020.
[6]. Ei:s forslag till tillforlitlighetsnorm for Sverige, Energimarknadsinspektionen, 2021.
[7]. European Resource Adequacy Assessment, ENTSO-E, 2021.

BIOGRAPHY

Jerneja Bogovič received B.Sc. and Ph.D. degrees in electrical engineering from the Faculty of Electrical Engineering, University of Ljubljana, Ljubljana, Slovenia, in 2011 and 2017, respectively. She is currently an assistant with the Faculty of Electrical Engineering, University of Ljubljana. Her areas of interest include power-system modeling and analysis and FACTS devices.

ICENS 8TH INTERNATIONAL CONFERENCE ON ENGINEERING AND NATURAL SCIENCE
May 18-22 2022 Istanbul (Hybrid Event)

An Investigation on Plan and Facade Characteristics of High-Rise Buildings

Eralp Kaya[1], Taner Ucar[2]

Abstract

High-rise buildings are an increasingly common type of commercial and residential buildings because of their large capacity on small lands. These buildings appear with different architectural features with the development of new building materials and technologies. In this study, plan shapes and facade forms used in high-rise buildings are investigated considering the ten tallest buildings in the world. Architectural characteristics of the considered high-rise buildings are briefly summarized based on the results of detailed investigations. Structural systems of the buildings are analyzed, particularly in plan shapes. As a result, it has been observed that different plan shapes and facade forms are determined based on building-specific reasons. High-rise buildings are designed with different architectural plan forms in accordance with the functional requirements. These plan forms are also created with various common areas to strengthen the relations of building users with each other. On the other hand, the most important factor in the current design practice of these forms is the wind load and the forms are generally designed considering the results obtained from wind tunnel analysis. The use of rounded lines in plan and facade forms allows the wind load affecting the building to decrease and the user's comfort to increase. Another important factor in the design is the creation of an aesthetic appearance on the exterior of the high-rise building. In particular, the facade forms of such buildings are designed in accordance with the design principles for increasing the aesthetic perception of the building, as well as the image of the city.

Keywords: High-rise buildings, aesthetic perception, wind load, plan shape, facade form.

1. INTRODUCTION

High-rise buildings are generally built in big cities and the number of these buildings is ever-increasing around the world. High-rise buildings are designed with different approaches in plan and facade forms as a result of the increase in building height. One of the most important factors dominating the design approach is the lateral loads caused by wind and earthquake ground motion. Excessive lateral loads acting on high-rise buildings directly affect the comfort and safety of building users. Therefore, the plan and facade forms of high-rise buildings are commonly designed to reduce the potential influence of lateral loads. In addition to structural considerations, the remarkable appearance of the building is another important factor affecting the design of high-rise buildings. As a result, these buildings are becoming the symbols of big cities, and therefore their aesthetic and striking appearance is an important issue to increase the prestige of the city.

The present study evaluates the plan and facade forms of the tallest high-rise buildings in the world. Accordingly, the ten tallest completed buildings in the world are studied. First, the plan shapes of the considered buildings are analyzed in particular and schematic plan views of different floors are drawn schematically by the Authors to clearly illustrate the structural forms. Afterward, facade forms obtained from Council on Tall Buildings and Urban Habitat database [1] are examined. Finally, plan and facade characteristics of the ten tallest completed high-rise buildings in the world are compared.

[1] *Dokuz Eylul University, The Graduate School of Natural and Applied Sciences, 35390, Buca/Izmir, Turkey.* eralp.kaya@ogr.deu.edu.tr

[2] *Corresponding author: Dokuz Eylul University, Department of Architecture, 35390, Buca/Izmir, Turkey.* taner.ucar@deu.edu.tr

2. PLAN CHARACTERISTICS OF HIGH-RISE BUILDINGS

There are some considerations commonly implemented in designing the plan of high-rise buildings. One of them is a symmetrical plan shape with a core in the middle. Some buildings have multiple cores inside and asymmetric plan shapes. However, designing the building with a symmetrical plan is more effective in terms of resistance to the lateral forces. Cores are vertical structural elements and, from an architectural point of view, they limit the area of usage in high-rise buildings. Designing a building with multiple cores leads to less usage area than that of a building with a single core. On the other hand, cores are very essential elements to be considered in the structural design of high-rise buildings. For mega tall buildings which are higher than 500 m, floor plan areas are generally observed to decrease.

Table 1 shows the different plans of the lower, middle, and upper floors of the ten tallest completed buildings in the world. All the plan shapes are drawn by the Authors. It is apparent from this table that each high-rise building has specific design aspects. However, some approaches are similar for some buildings. The plan shape of the seven buildings is square or rounded square whereas the other three buildings, Burj Khalifa, Shanghai Tower, and Makkah Royal Clock Tower, stand out with their different plan shapes. Burj Khalifa building has a Y-shaped plan [2]. This plan form provides an advantage in increasing the facade ratio of the building, as well as the resistance against lateral loads. Shanghai Tower has a double-skinned facade system. The form of this facade provides developing atriums at every 12- to 15-floor level and these floors are designed in the shape of triangles. Plans of the other floors are in the shape of a circle [3]. Makkah Royal Clock Tower has a rectangular form and the upper floor plan is not presented in Table 1 since the mechanism of the world's highest clock is located on the upper floor [4].

Three of the listed buildings have sharp corners and straight edges, while the other buildings have rounded corners, concave and convex edges. One World Trade Center stands out with a different design from other buildings. In the plan of this building, the edges are straight, while the corners are chamfered. As the height of the building increases, the corners of the core form are also chamfered [5].

As a result of increase in height of many high-rise buildings, the floor areas become narrow and the building becomes slender. However, in CITIC Tower, the smallest floor area is on the middle floor. The floor area of the building decreases from the ground floor to the middle floor and increases from the middle floor to the top floor. The design of this building was inspired by the "zun" shape that emerged during the Bronze Age of China [6].

On the upper floors of high-rise buildings, the facade is exposed to severe wind loads. For this reason, spaces such as balconies and terraces that open to the outside are generally not designed on the upper floors of high-rise buildings. In Burj Khalifa and Guanzhou CTF Finance Center, terrace areas are created by setbacks. In Burj Khalifa building, terraces have been created by making 9 m setbacks at every seven floors and wind sensors have been used to ensure safe access to these terraces [2]. In this way, more opportunities are provided for building users to have fresh air in open space.

3. FACADE CHARACTERISTICS OF HIGH-RISE BUILDINGS

Different approaches have been used in the design of tall buildings throughout history. Before the development of new structural systems and materials with high resistance and deformation capacity, masonry structural systems were frequently used in high-rise buildings. The ground floor walls of these buildings were very thick and these thick walls occupy a lot of space in floor areas. With the development of new structural materials, structural elements begin to occupy less space in the floor plan. At the beginning of the 20th century, these structural elements were also shown on the facade as a design approach of this period. At the end of the 20th century, design approaches that give a mechanical appearance were applied to the facades of high-rise buildings [7]. In the 21st century, glass curtain wall systems are commonly used in high-rise buildings. It is observed that the facades of the all buildings investigated in this study are also designed with glass cladding.

Mega-tall buildings often become thinner as a result of height increase. Therefore, the mass of the building reduces and inertia forces tend to decrease. The facade forms of the world's ten tallest completed buildings are shown in Table 2, where the total height (H_N) and the floor numbers (N) are also given. It can be seen from the data in Table 2 that except for CITIC Tower, every building tapers as it rises. However, the tapering rates and zones are different for each building. Burj Khalifa building has setbacks on certain floors and it is the building with the highest ratio of ground floor area to upper floor area. In Shanghai Tower, designers decided a scaling of 55% from base to top according to the analysis. Analyses are also conducted for the rotation ratio and 120° is found to be the optimum rotation angle of the building [8].

Table 7. Floor plans of the considered high-rise buildings

Building name	Lower floors	Middle floors	Upper floors
Burj Khalifa			
Shanghai Tower	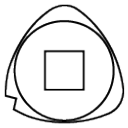		
Makkah Royal Clock Tower	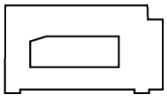	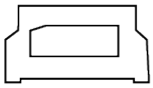	–
Ping an Finance Center	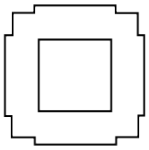	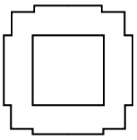	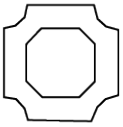
Lotte World Tower	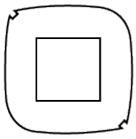	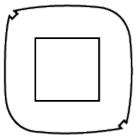	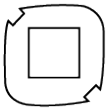
One World Trade Center	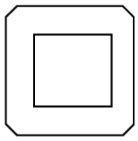	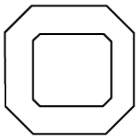	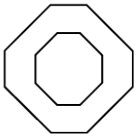
Guanzhou CTF Finance Center	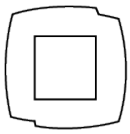		
Tianjin CTF Finance Center	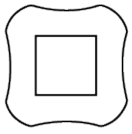	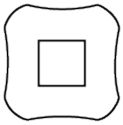	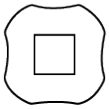
CITIC Tower	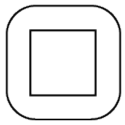		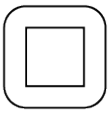
Taipei 101	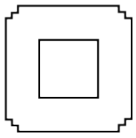	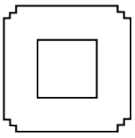	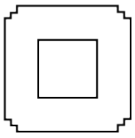

Makkah Royal Clock Tower and TAIPEI 101 have the architectural and cultural traces of the region where they are built. Makkah Royal Clock Tower is the tallest clock tower in the world and has a huge crescent at its top. The Taipei 101 building was designed with inspiration from the pagoda architecture and motifs from the Chinese culture were used on the facade of the building [9]. In the facade form, Taipei 101 tapers from the ground floor to a certain height. On the other hand, Makkah Royal Clock Tower and Lotte World Tower were continued with the same floor area up to a certain height from the ground and then tapered. Furthermore, the Lotte World Tower form was inspired by the historical Korean arts of ceramics, porcelain, and calligraphy. The building's curvilinear form and its slender conical form reflect Korean craftsmanship [10]. In the facade designs of Ping an Finance Center and Tianjin Tower, the structural system elements are emphasized on the facade. The braced or curvilinear forms of some structural elements are determined in accordance with the analysis. The word “ping” in Chinese means peace and security, and Ping an Finance Center is designed to give the image of a safe building.

The facade design of One World Trade Center was inspired by the tapering triangular forms of the Chrysler Building and Empire State buildings, which are the important buildings of the city. As the height of the building with cubic floor area increases, its corners are chamfered, resulting in a facade design consisting of eight isosceles triangles.

Table 8. Elevations and perspectives of the considered high-rise buildings

Building name	Burj Khalifa	Shanghai Tower	Makkah Royal Clock Tower	Ping an Finance Center	Lotte World Tower	One World Trade Center	Guanzhou CTF Finance Center	Tianjin CTF Finance Center	CITIC Tower	Taipei 101
N	163	128	120	115	123	94	111	97	109	101
H_N (m)	829	632	601	599.1	554.5	541.3	530	530	527.7	508
Elevation	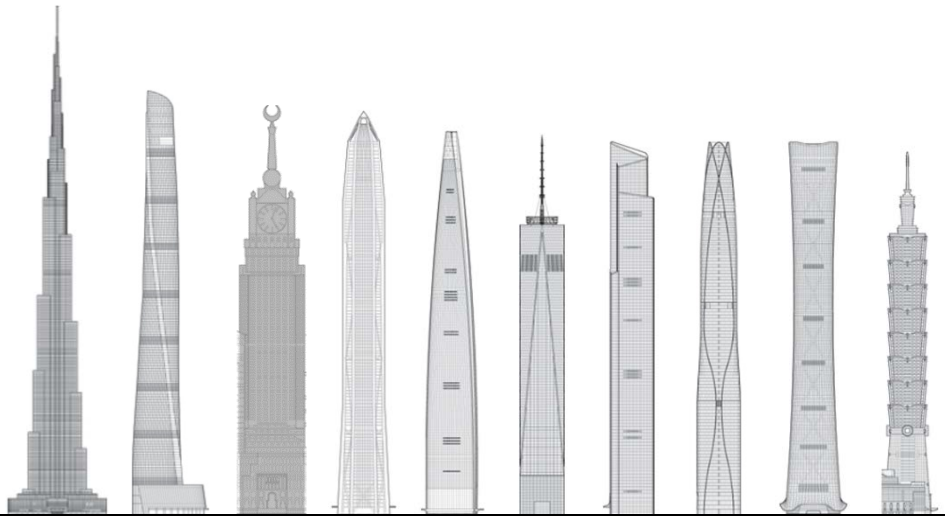									

4. SUMMARY AND CONCLUSIONS

In this study, the design approaches regarding the plan shape and facade form of the ten tallest completed buildings in the world are examined and compared. The results of this study indicate that the most common plan shape is square. Moreover, the other high-rise buildings have Y-, circular, and rectangular plan shapes. Rounding the sharp corners of symmetrical shapes is a more accurate approach, but sharp corners are also used in some buildings. The chamfered corner design is frequently preferred. Based on the results of wind analysis, it has been understood that the use of rounded or chamfered corners instead of sharp corners reduces the wind loads on the building and increases user comfort. It has been observed that concave and convex edge designs are preferred in some buildings in plan form. This design approach has been determined in accordance with the conducted analyses, as well as the aim of obtaining an aesthetic appearance. It has been observed that the floor areas of the buildings decrease as a result of the increase in height, and only CITIC Tower has a different design approach in this regard. The results of the investigation on the facade forms of buildings reveal that a design approach that is tapered as a result of the increase in height has been preferred. This approach decreases the building mass and the inertia loads acting on the structural system. The facades of the buildings are designed with glass curtain walls and the structural system elements of some buildings are emphasized on the facade. Approaches reflecting the cultural and architectural characteristics of the region where the building was built are also apparent. Floor terraces are created with setbacks and the relationship of building users with the outside is strengthened. Shanghai Tower stands out with a different approach from other buildings, which is a 120° rotating facade form. Finally, it can be concluded that high-rise buildings are designed in accordance with the requirements of the country or region where they are built. The designs are dominated by analyses that measure the effect of lateral loads on the building. The differences and similarities mentioned above for the ten tallest buildings of today will continue in the tall buildings to be built in the future. More different design approaches will be possibly as a result of the developing technology and the number of high-rise buildings will gradually increase.

REFERENCES

[1]. (2022) CTBUH website. [Online]. Available: https://www.ctbuh.org/
[2]. F. Durie, “Burj Khalifa: Creating the world’s tallest integrated “vertical city”, in Proc. CTBUH 2012 9th World Congress, 2012, pp. 78–81.
[3]. J. Xia, D. Poon, and D. Mass, “Case study: Shanghai Tower”, CTBUH Journal, vol. 2010, pp. 12–19, 2010.
[4]. A. Osman, and C. Malak, “Evaluating the stresses in a supertall structure: Field monitoring and numerical analysis”, in Proc. 4th Conference on Smart Monitoring, Assessment and Rehabilitation of Civil Structures, 2017.
[5]. K. Lewis, and N. Holt, “Case study: One World Trade Center, New York”, CTBUH Journal, vol. 2011, pp. 14–19, 2011.
[6]. L. Peng, C. Yu, and Z. Song, “The structural design of “China Zun” Tower, Beijing”, International Journal of High-Rise Buildings, vol. 5, pp. 213–220, 2016.
[7]. Z. Y. Harmankaya, and A. Soyluk “Structural system-facade interaction in high-rise buildings”, in Proc. 5th National Symposium on Roof and Facade, 2010, (in Turkish).
[8]. L. Xia, “The parametric design of Shanghai Tower’s form and facade”, in Proc. CTBUH 2012 9th World Congress, 2012, pp. 112–119.
[9]. I. Kourakis, “Structural systems and tuned mass dampers of super-tall buildings: Case study of Taipei 101”, Massachusetts Institute of Technology, Department of Civil and Environmental Engineering, Thesis (M. Eng.), 2007.
[10]. (2022) KPF website. [Online]. Available: https://www.kpf.com/projects/lotte-world-tower

ICENS 8TH INTERNATIONAL CONFERENCE ON ENGINEERING AND NATURAL SCIENCE
May 18-22 2022 Istanbul (Hybrid Event)

Effect of Nozzle Tip Geometry on Drop Diameter Falling Down String

Bora Dogan[1], Ismail Teke[2]

Abstract

The creation of sequential droplets that fall through a vertical string at a specific period without any clash and maintaining the same pace is an ideal condition for any heat/mass transfer calculation as the entire system can be deemed stagnant. The available investigations to create those sequential droplets on vertical string mainly focus on flow rate and nozzle diameter. Contrary to prior studies, this investigation focuses on the effect of the nozzle tip geometry on droplet generation along vertical string while keeping constant flow rate and nozzle diameter. The nozzle tip geometry has been modified to form different droplet diameters while considering the fundamentals of droplet generation. The changes in droplet diameters, which flow down the vertical string for each specific nozzle tip geometry, were investigated experimentally. All results and findings have been presented in this paper.

Keywords: *Droplet generation, Nozzle tip geometry, Flow down string, Film flows*

1. INTRODUCTION

Thin film flows that fall down on a vertically oriented highly curved surface cannot keep film form due to interfacial dynamics. The wave pattern begins to occur while film falls. Then with raise of wave amplitude that patterns turns into droplets. This phenomenon is known as Rayleigh Plateau Instability.

Due to shape of droplet, we accept as sphere, has high surface to volume ratio which increases heat and mass transfer rate on process applications. That opportunity grabs attention of researchers to design effective heat-mass transfer systems. The humidification-dehumidification, desalination systems [1], carbon-dioxide removal from fue gases [2][3][4], heat recovery systems [5][6] or other heat-mass transfer systems can be some of the examples usage of that phenomena.

One of the first studies done on that topic is from 19th century by Lord Rayleigh [7] in which Lord Rayleigh defines wave formations on long cylinder. Over years that phenomena keep popularity and searchers begin to define details of wave patterns and flow regimes. Kliakhandler et al. [8] one of the first researchers defined distinct flow regimes on this phenomena. They defined three distinct flow regimes;

1) Droplets flow down highly curved surface periodically and with same diameter. Those droplets do not clash or merge with each other and continues to flow while keeping to same distance to each other. That regime has been named as Rayleigh-Plateau Regime.

2) Droplets are irregular, which has different diameters. That creates aperiodic droplet flow which clash or merge during the flow. That regime has been named as Convective Regime.

3) Waves are unbalanced, that unbalance form really distinct diameter droplets. That regime is named as Isolated Droplet Regime.

Because of unsteady droplet patterns on second and third items, calculating heat and mass transfer not practical. However on Rayleigh-Plateau regime, where droplet diameters are same, distances between droplets are same and speed of the droplets are constant, situation is totally different. As all this variables are constant we can

[1]*Corresponding author: Yildiz Technical University, Department of Mechanical Engineering, 34349, Besiktas/Istanbul, Turkey. bordogan@hotmail.com*

[2]*Yildiz Technical University, Department of Mechanical Engineering, 34349, Besiktas/Istanbul, Turkey. iteke@yildiz.edu.tr*

name that flow as static compare to other regimes. That is the main reason researchers on that topic mainly focus on Rayleigh-Plateau Regime.

Also some researchers studies on nozzle diameter and how it effected on droplet diameter. Sadeghpour [9] experimentally studied how nozzle diameter effected droplet diameter, additionally Ji [10] generated an analytical model on that and reported that it has good alignment with Sadeghpour's experimental results.

While mentioning droplets we also talk about droplet generation. Tate [11] is one of the first researchers' works on pendant droplets. By using the force balance of pendant droplet on nozzle tip, Tate creates an equation which has been known as Tate's law or drop weight/volume method.

$$\sigma = \frac{mg}{2\pi r} \tag{1}$$

After Tate's study, Harkins and Brown [12] also investigates similar topic experimentally. When they try to verify their experimental results with drop weight method they find a miss match. Then they suggest a correction factor which named as F. With that arrangement drop weight method becomes;

$$\sigma = \frac{mgF}{2\pi r} \tag{2}$$

In the view of such information, we have experimentally investigated the effect of nozzle tip on droplet diameter to create periodical droplet, Rayleigh Plateau regime, through highly curved vertical surfaces.

2. EXPERIMENTAL METHODOLOGY

2.1 Experimental Setup

The experimental setup we designed to investigate nozzle tip effect on periodical droplet generation is presented in Figure 1. Basically to explain; liquid feeding system send our liquid to our specifically designed nozzles, a cotton string passes through center of the nozzle in vertical position. A high speed camera is placed to collect data at nozzle tip.

In the view of such information, we have experimentally investigated the effect of nozzle tip on droplet diameter to create periodical droplet, Rayleigh Plateau regime, through highly curved vertical surfaces.

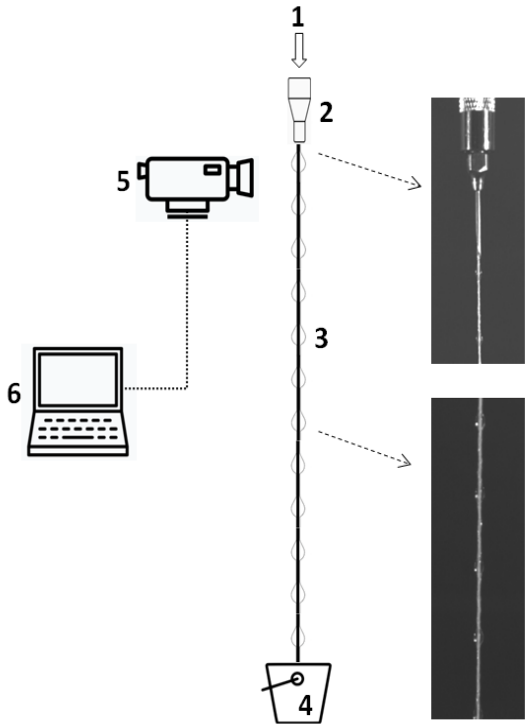

Figure 2. Schematic of the experimental system

Key factor in this set up is nozzles. The nozzles used on experimental setup are similar, similar ID and OD, similar material, however nozzles tips are modified as seen Figure 2,

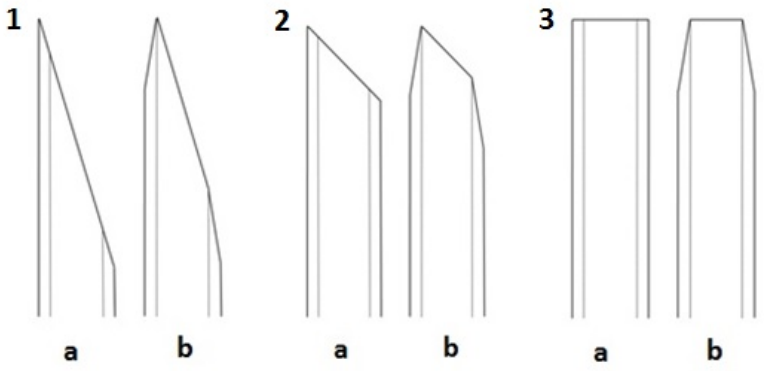

Figure 3. Inlet nozzle types. (a) Diagonal cut, (b) Diagonal cut with chamfer. (1) Diagonal cut 15 ^{0}, (2) Diagonal cut 45 ^{0}, (3) Diagonal cut 90 ^{0}.

Figure 4. Nozzle sample used in the experimental setup

2.2 Experimental Phase

The experimental equipments are been placed on vertical test bench. The liquid feeder system has been set to mass flow rate 0,05g/s and connected to nozzle. All six different nozzles placed one by one with two different cotton thread diameter 0,5mm and 0,35mm.

High speed camera placed and focused on nozzle tip with 180mm lens whose frame rate set to 600fps. Camera has been connected to PC via Phantom Camera Control Application.

For each nozzle and cotton thread, in combined 12 test combination, data has been collected and presented in next chapter.

3. RESULTS AND DISCUSSION

The data collected with our camera has been send to Phantom Camera Control Application for post process. The diameters of droplets generated by 6 different nozzle and 2 different thread diameter have been identified. As expected for each condition our nozzles have been generated different droplet diameters.

Also we have identified;

- The change of cotton thread effects the droplet diameter. When cotton thread diameter gets smaller, droplet diameter increases. It can be explained as the open gap between ID and thread gets larger when thinner thread used, so nozzle generates bigger droplets.
- Adding a chamfer on nozzle tip also supported to change droplet diameter. As the chamfer reduces the interface area between droplet and nozzle, so that when we add chamfer droplet diameter got smaller.
- The angular cut also effects droplet diameter. The tip point get sharper, when angular cut angle gets smaller, droplet diameter also get smaller. This situation is totally opposite than we expected, as interface area get bigger between nozzle and droplet, droplet diameter could be bigger. However it has been visualized that when droplet begins to cumulate on tip then begin to accelerate due to angular cut. So that when cut angle is smaller (tip is sharper), droplet diameter gets smaller.

That can be easily seen at Figure 4.

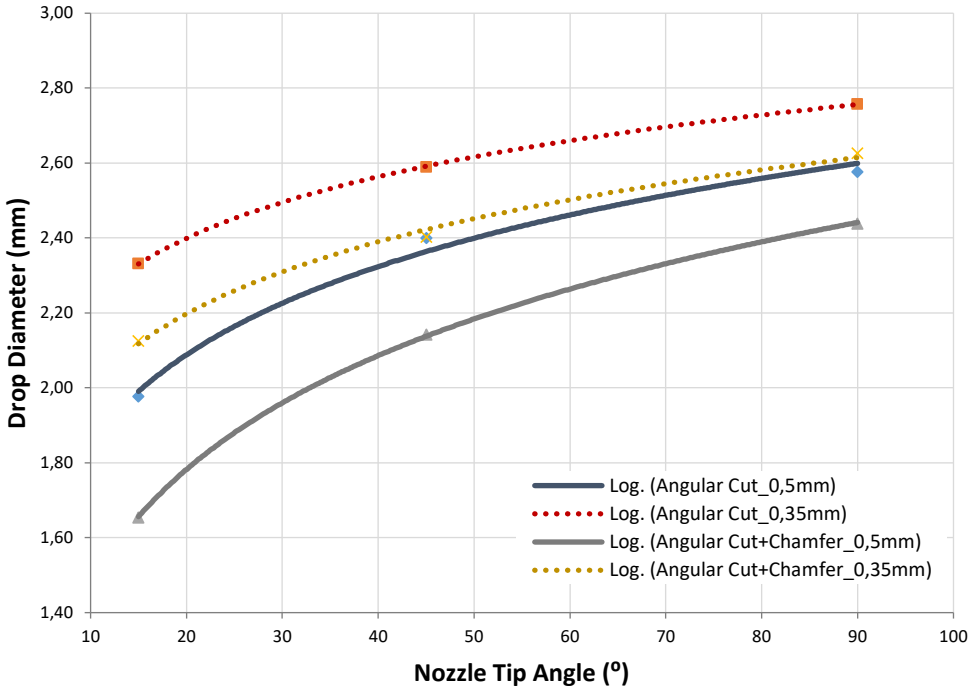

Figure 5. Drop diameter change with different nozzle configurations

4. SUMMARY AND CONCLUSION

In this study, series of experiments has been done to understand how the nozzle tip geometrical change effect droplet diameter falling through vertical thread. With implemented geometrical modifications on nozzle tip, differentiation of the droplet diameters achieved while keeping other parameters such as mass flow, nozzle internal and outer diameter.

We have find out that change of the nozzle tip effects droplet diameters directly. As the mass flow is constant, with change of the droplet diameter that also changes frequency of droplet generation. So that frequency of the droplets can be also controlled by nozzle tip.

We can summarize our findings below,

- Adding a chamfer on nozzle and modifying tip geometry effects droplet diameters. The chamfer added nozzle generates smaller diameter compare to the one which is not added.
- The cutting nozzle tip angularly also effects droplet diameters generated on nozzle tip. Although the surface area on the nozzle tip enlarges, droplet size gets bigger cut angle get bigger (nozzle tip gets sharper). We have visualized through our experiments that, due to angularity liquid begins to accelerate towards to nozzle tip, where is pointy. That pointy edge and acceleration pushes droplet to fall earlier before it gets bigger. So we can say that, when nozzle tip get sharper, droplet diameter gets smaller.
- As mass flow is same, different diameters of droplets generated effects frequency of the droplets fall through the thread. When droplets get smaller frequency is increase.

REFERENCES

[1]. Sadeghpour, A., Zeng, Z., Ji, H., Dehdari Ebrahimi, N., Bertozzi, A. L., & Ju, Y. S. (2019). Water vapor capturing using an array of traveling liquid beads for desalination and water treatment. Science advances, 5(4), eaav7662. https://doi.org/10.1126/sciadv.aav7662

[2]. Uchiyama, K., Migita, H., Ohmura, R., & Mori, Y. H. (2003). Gas absorption into "string-of-beads" liquid flow with chemical reaction: Application to carbon dioxide separation. International Journal of Heat and Mass Transfer, 46(3), 457-468. https://doi.org/10.1016/S0017-9310(02)00301-0

[3]. H. Migita, K. Soga, Y. H. Mori, Gas absorption in wetted-wire column, AIChE Journal (2005), 51 (8), 2190-2198, https://doi.org/10.1002/aic.10483

[4]. Hosseini, S., Alizadeh, R., Fatehifar, E., Alizadeh, O., (2014). Simulation of gas absorption into string-of-beads liquid flow with chemical reaction. Heat and Mass Transfer. 50. 1-11. 10. doi: 1007/s00231-014-1343-z.

[5]. K. Hattori, M. Ishikawa, Y. H. Mori, Strings of liquid beads for gas-liquid contact operation, AIChE Journal (1994), 40 (12), 1983-1992, https://doi.org/10.1002/aic.690401209

[6]. T. Nozaki, N. Kaji, Y. Mori, Heat transfer to a liquid flowing down vertical wires hanging in a hot gas stream: A n experimental study of a new means of thermal energy recovery., HEAT Transfer (1998), 6, 63-68, https://cir.nii.ac.jp/crid/1574231874866716160

[7]. Rayleigh, L. On The Instability of Jets. Proceedings of The London Mathematical Society, 1, 4-13, https://doi.org/10.1112/plms/s1-10.1.4

[8]. Kliakhandler, I., Davis, S., Bankoff, S. (2001). Viscous beads on vertical fibre. Journal of Fluid Mechanics, 429, 381-390. doi:10.1017/S0022112000003268

[9]. Sadeghpour, A., Zeng, Z., & Ju, Y. S. (2017). Effects of Nozzle Geometry on the Fluid Dynamics of Thin Liquid Films Flowing down Vertical Strings in the Rayleigh-Plateau Regime. Langmuir: the ACS journal of surfaces and colloids, 33(25), 6292–6299. https://doi.org/10.1021/acs.langmuir.7b01277

[10]. Ji, H., Sadeghpour, A., Ju, Y., & Bertozzi, A. (2020). Modelling film flows down a fibre influenced by nozzle geometry. Journal of Fluid Mechanics, 901, R6. doi:10.1017/jfm.2020.605

[11]. T. Tate Esq. (1864) XXX. On the magnitude of a drop of liquid formed under different circumstances, The London, Edinburgh, and Dublin Philosophical Magazine and Journal of Science, 27:181, 176-180, DOI: 10.1080/14786446408643645

[12]. W.D. Harkins, F.E. Brown, Determination of surface tension (Free surface energy), and the weight of falling drops: The surface tension of water benzene by capilary height method., Journal of American Chemical Society (1919), 41 (4), 499-524, https://doi.org/10.1021/ja01461a003

ICENS 8TH INTERNATIONAL CONFERENCE ON ENGINEERING AND NATURAL SCIENCE
May 18-22 2022 Istanbul (Hybrid Event)

Optimization of the Cooling Parameters of a 250 kW PMSM by Taguchi Method

Mert Bedirhan Genc[1], Rami Habash[2], Gamze Gediz Ilis[3]

Abstract

In this study, a nine-phase, 250 kW Permanent Magnet Synchronous Motor (PMSM) was considered, and both the magnetic and thermal models of this motor with heat losses are studied. The motor is cooled by the refrigerant fluid over the parallel fixed channels on the fixed stator. The mass flow rate of the coolant, the pipe diameter of the coolant pipe, the number of turns of this pipe, the type of the refrigerant, and the change of the torque value are analyzed by using the Taguchi Method in order to optimize the motor thermal system. After Taguchi analysis of these parameters, the results showed that increasing the mass flow rate of the refrigerant has a significant effect on the winding temperature. By increasing the torque of the motor, the winding temperature increases. The results showed that A4B1C3D3E4 (mass flow rate (A)=50 kg/h pipe diameter (B)=17.7 mm, number of turns (C)=20, type of fluid (D)= EGW50/50, torque (E)=2000 Nm) is the best cooling design parameters for the cooling strategy of the PMSM.

Keywords: PMSM, Thermal Model, Magnetic Model, Efficiency, 3D Parametric Design, Cooling Methodology

1. INTRODUCTION

Nowadays, Permanent Magnet Synchronous Motors (PMSM) are researched for the development of electric motors to work more efficiently with electric vehicles. PMSMs can be classified according to their mechanical and electrical topologies. PMSM can be shown as the most efficient motor among all motor types, with their unique structures to provide high torque values at high rpm values. It has higher efficiency values by showing higher performance at lower motor volumes compared to motor types with the same power.

The biggest problem of electric motors is the serious decrease in efficiency out of the ideal operating temperature. In response to variable ambient temperature or sudden torque and power demands, a sudden temperature increase occurs. In this study, a nine-phase, 250 kW PMSM was considered, and both the magnetic and thermal models of this motor with heat losses are studied. It is aimed to improve the motor efficiency, which is cooled with refrigerant through the fixed parallel channels on the stator, by changing the critical variables determined on the cooling jacket.

As a result of this study, the life span of the mechanical parts that make up the motor and the efficiency of the motor will increase when the motor works at the ideal operating temperature.

2. LITERATURE REVIEW

Literature reviews showed that cooling systems are depending on the motor's power as summarized in Figure 1. Air is generally used for cooling under 40kW power, on the other hand, water-cooled systems are frequently used for motors over 40kW power range. In this study, the unique features that distinguish these works are the 9-phases, outer rotor topology, and 250kW maximum power.

There are many studies can be found from the literature survey which is focusing on the cooling strategy of the motors not only limited with air or water coolant but also related with the system design and the thermal system

[1]*Corresponding author: Gebze Technical University, Department of Mechanical Engineering, 41400, Gebze/Kocaeli, Turkey. m.genc2020@gtu.edu.tr*

[2] *Istanbul Okan University, Department of Mechatronic Engineering, 34959, Tuzla/Istanbul, Turkey ramihabash@live.com*

[3] *Gebze Technical University, Department of Mechanical Engineering, 41400, Gebze/Kocaeli, Turkey. ggediz@gtu.edu.tr*

improvement of the vehicles. In the study of Sun et al. [18], concluded that the design considerably reduces the cost of the coolant structure when the temperature performance of the motor increases in the tested and simulated model the motor tested to obtain outlet temperature with different flow ratios at 5000 rpm, 101 Nm, and water temperature 55ºC. And then the better combinations were obtained when the constant was changed. The thermal model in the study of Satrústegui et al. [21] was used in to obtain variables for the main parameters that define the water jacket and the shaft. Firstly, the topology of the water jacket was analyzed to create a thermal model, and it was compared that the other topologies are spiral, U-shaped (single channel), U-shaped (bifurcated), and axial. As a result, the study importantly reduced the temperatures of some motor parts. In the study of Putra and Ariantara [2], the heat pipes are L-shaped and placed on the surface of the motor housing. In this way, installation and maintenance are effortlessly obtained by the new topology. The focus of this study is to provide better performance of the electric motor thermal management system by heat pipes. In the paper of Staton et al. [3], the effect of different cooling arrangements was studied in order to find out the impact of the frame openings and the rotor end-ring wafters on the end-winding cooling. The measured temperature increase is used to estimate the heat transfer between end-windings and external frame, by the help of the considered cooling arrangements. Results of these prototypes are compared with calculated results via thermal networks.

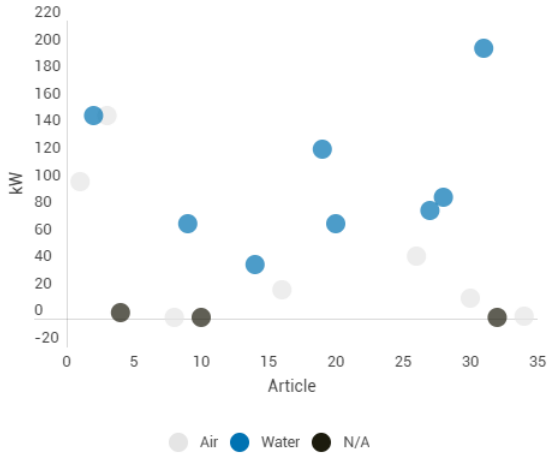

Figure 1. Motors Power rating according to refrigerant types in Literature review [1-35].

As given in above, the studies in the literature is limited which are focusing on the cooling design of the motor. In this study, in order to improve the performance of the cooling structure of the PMSM, the heat transfer of the Cooling Jacket (CJ) is analyzed with many variables such as the mass flow rate of the coolant, the pipe diameter of the coolant pipe, the number of turns of this pipe, the type of the refrigerant, and the change of the torque. The optimization of these variables are performed and the average winding temperature is analyzed in this study. By optimization of the mass flow rate of the coolant, the pipe diameter of the coolant pipe, the number of turns of this pipe, the type of the refrigerant, and the change of the torque, the best cooling design is obtained.

3. THE COOLING JACKET DESIGN

Fig. 2 presents the view of the cooling jacket with the single flow pipeline. The cooling jacket is placed stator inner surface which is close to the winding. The refrigerant fluid which is at 45 °C (for cooling) is flowing inside of the single flow pipe for cooling. The cooling jacket exchanger is cooled via a single pipe. During the cooling process, the refrigerant fluid starts to flow from the cooling jacket pipes.

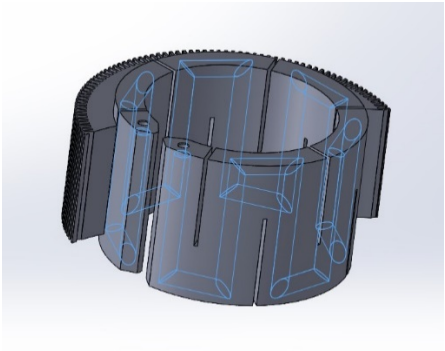

Figure 2. Motor Cooling Jacket Cross Section and the One Single Pipe Line.

As illustrated in Figure 3, the motor cross-section is shown where the shaft temperature is constant. The green-colored side is the cooling jacket, the hottest spot seen is the winding parts colored in red which is the hottest region. The light blue represents the rotor temperature, and the dark blue color shows the motor casing temperature which is located outer side of the motor. The maximum and the minimum temperatures for the current design of the motor are found 98 and 75 °C, respectively. In this analysis, the outlet temperature of the refrigerant fluid of the motor at constant 900 rpm is plotted and shown in Figure 4. The outlet temperature of the refrigerant, which the inlet temperature is assumed to be constant at 45 °C, was measured as 54.9°C at 900 secs later at constant 900 rpm motor speed. The result which is found by numerical modelling has been validated by the experimental data with a %4 margin of error.

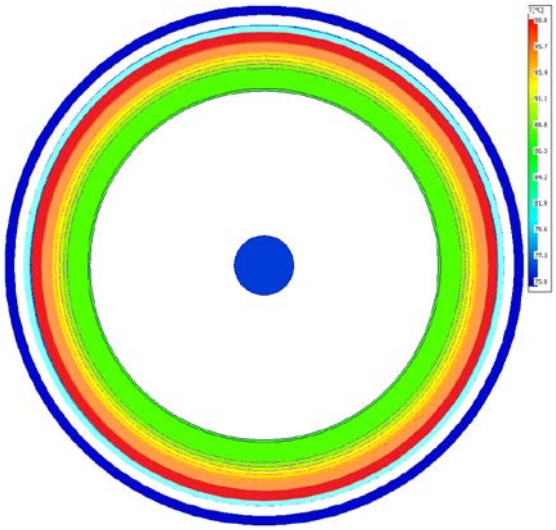

Figure 3. Thermal distribution of the Motor for the first time.

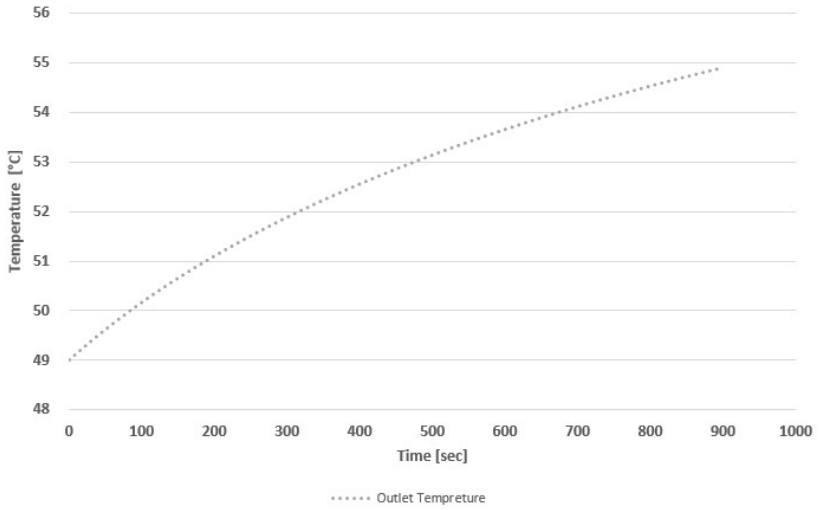

Figure 4. The Temperature of the Outlet Refrigerant Fluid at between 0 sec to 900 sec.

The current motor has cooling jacket coolant with a mass flow rate of 20 L/min, the pipe diameters of the coolant pipe of 25.4 mm with 12 number of turns in the stator region. The type of the refrigerant of this coolant is EGW 60/40. There are four main geometrical parameters are taken into account to develop the cooling jacket design such as; Mass flow rate (A), Pipe diameter (B), Number of turns (C), Type of the coolant fluid (D), and the Motor torque (E).

The parameters and the change of their values are summarized in Table 1. Mass flow rate (A), Pipe diameter (B) and the Number of turn of the cooling pipe (C), the Motor torque (E) parameters are changed in values. On the other hand, for the parameter which refers the Types of coolant fluid (D) are taken as; EGW60/40, PGW60/40, EGW50/50, and Therm. The specified diameter sizes are referenced from the commonly used brass pipes. Referenced dimensions have corresponded from inch to mm. The parameters are chosen for developing the cooling strategy of the motor by only changing the design parameters of the cooling pipe of the PMSM.

To optimize the cooling strategy for best cooling design, the Taguchi Methodology is performed in this study. Taguchi L16 orthogonal array is implemented L16 (4^5) for different 5 factors (A-E) each has 4 different values (levels). 4^5 runs should be performed to analyze the results. Thanks to Taguchi method the number of runs reduces to 16 to optimize the cooling strategy of the motor. Factors determined as stated above variables are analyzed by using the Taguchi Method as shown in Table 1. As illustrated in Table 2, Taguchi created 16 runs with these levels and factors. After that, these 16 runs were analyzed by using Motor CAD. As a result of these runs, the CJ outlet and average winding temperatures were calculated and the results are given in Table 2.

Table 1. Factors &Levels in Taguchi Method.

Factor Information

Factor	Type	Levels	Values
Mass Flow Rate	Fixed	4	20; 30; 40; 50
Pipe Dia	Fixed	4	17,7; 19,0; 25,4; 31,7
Number of Turns	Fixed	4	12; 16; 20; 24
Type of Fluid	Fixed	4	EGW60/40; PGW60/40; EGW50/50; THER
Torque	Fixed	4	500; 1000; 1500; 2000

Table 2. Taguchi Iterations and Results.

Iterations	Mass Flow Rate [L/min]	Pipe Dia[mm]	Number of Turns	Type of Fluid	Torque[Nm]	Shaft Speed [rpm]	CJ INLET TEMP[°C]	CJ OUTLET TEMP[°C]	WINDING TEMP (AVG) [°C]
1.	20	17.7	12	EGW60/40	500	3422	49	57.89	122.71
2.	20	19	16	PGW60/40	1000	2359	49	57.31	104.10
3.	20	25.4	20	EGW50/50	1500	1554	49	55.64	88.12
4.	20	31.7	24	THER	2000	1106	49	50.40	97.85
5.	30	17.7	16	EGW50/50	2000	1106	49	57.45	80.79
6.	30	19	12	THER	1500	1554	49	56.75	104.42
7.	30	25.4	24	EGW60/40	1000	2359	49	54.55	96.28
8.	30	31.7	20	PGW60/40	500	3422	49	54.07	120.51
9.	40	17.7	20	THER	1000	2359	49	57.75	103.74
10.	40	19	24	EGW50/50	500	3422	49	54.31	114.01
11.	40	25.4	12	PGW60/40	2000	1106	49	53.24	91.07
12.	40	31.7	16	EGW60/40	1500	1554	49	53.84	86.14
13.	50	17.7	24	PGW60/40	1500	1554	49	54.01	82.36
14.	50	19	20	EGW60/40	2000	1106	49	54.86	77.22
15.	50	25.4	16	THER	500	3422	49	55.39	122.61
16.	50	31.7	12	EGW50/50	1000	2359	49	53.01	96.89

In order to obtain the best results, the lowest winding temperature is required for the cooling jacket. Therefore, the smaller the better method in Taguchi method is used for the Average Winding Temperature. The Taguchi analysis created the plot in Figure 5. The effects of five design parameters on the cooling jacket are plotted in Figure 5. As seen for this figure, the smallest values of each factors should be taken for the lowest average winding temperature. And also, these points corresponding values are shown in Table 3. As seen these values on the chart to obtain the best thermal design for Cooling Jacket as mass flow rate (A); 50 l/min, the pipe diameter (B); 17.7mm, the number of turns (C); 20, the type of fluid (D); EGW 50/50, and the torque (E); 2000 Nm give the lowest winding temperature. Thus, A4B1C3D3E4 can be defined as the best cooling design for a cooling jacket.

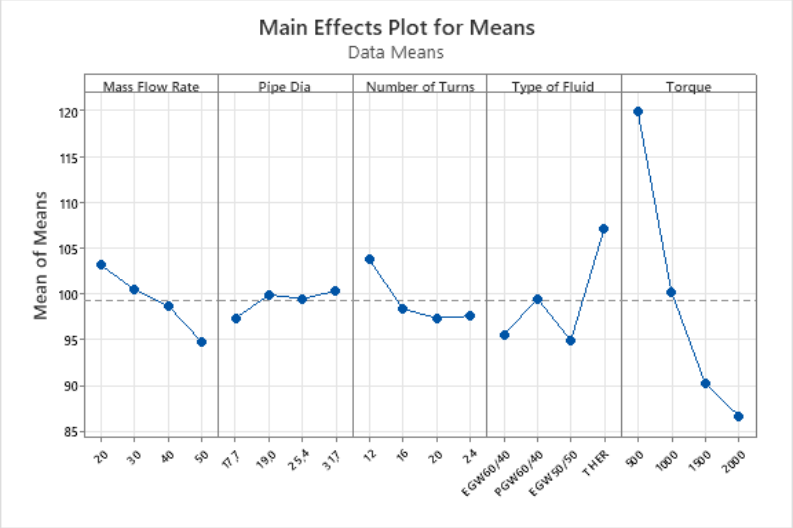

Figure 5. The Plot of the Main Effect per Levels for Means.

Table 3. Results of the Means.

Response Table for Means

Level	Mass Flow Rate	Pipe Dia	Number of Turns	Type of Fluid	Torque
1	103,19	97,40	103,78	95,59	119,96
2	100,50	99,94	98,41	99,51	100,25
3	98,74	99,52	97,40	94,95	90,26
4	94,77	100,35	97,62	107,16	86,73
Delta	8,42	2,94	6,38	12,20	33,23
Rank	3	5	4	2	1

4. RESULTS AND DISCUSSION

This study aims to optimize the cooling jacket design for the best cooling performance of a PMSM. In order to obtain the intended results, the 3D cooling jacket design is considered for this study. The L16 orthogonal array values are calculated for predicting the best configuration. Iterations of the cooling jacket have an effect on average winding temperature and the found results of the cooling jacket and average winding temperature iteration results are given in Table 2. These results is used for the best design. The optimization of the best configuration values was obtained as; Mass flow rate (A): 50 L/min, Pipe diameter (B):17.7 mm, Number of turns (C): 20, Type of the coolant fluid (D): EGW50/50 , and the Motor torque (E): 2000 Nm which is 1106 rpm.

As mentioned above, A4B1C3D3E4 design is the best cooling design for a cooling jacket. On the other hand, the worst case is found as A1B4C1D4E1 where the Mass flow rate (A1) is 20 l/min, the Pipe diameter is 31.7mm (B4), the number of turns is 12 (C1), type of fluid is Therm (D4), and torque value is 500 Nm (E1).

As illustrated in Figure 6. the thermal distributions of the motor cross-section are given for the current (A1B3C1D1E4), worst (A1B4C1D4E1), and best (A4B1C3D3E4) models, respectively.

The current model of the motor shown in Figure 6. has high and cold spot temperatures of 98°C and 75°C. The best model in Figure 6. has a hot spot temperature of 79°C while the cold spot temperature is 58 °C. The worst model of the motor has 159°C and 76°C as max and min temperatures. The cold spot temperature decreased to 54 °C from 75°C. The hot spot temperature decreased to 79 °C from 98 °C when compared to best and current models.

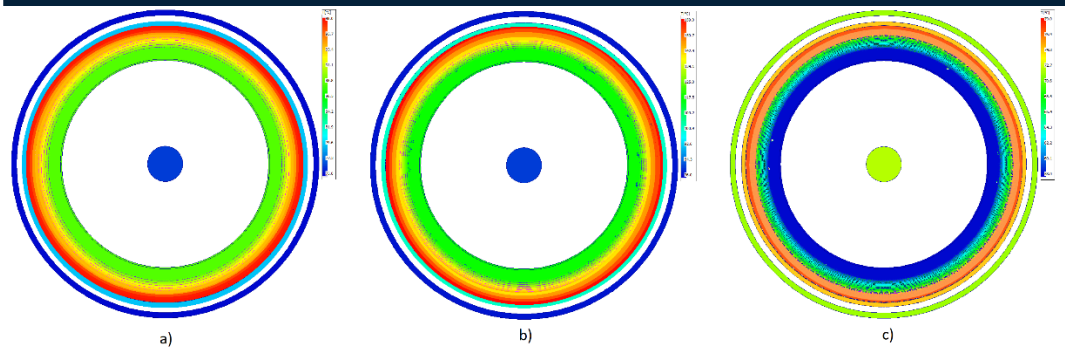

Figure 6. Thermal distribution of the a) Current, b) Worst and c) Best design, respectively.

The created thermal models of the motor were compared according to the temperature of the cooling jacket and winding average temperature changes respectively shown in Figure 7 and Figure 8.

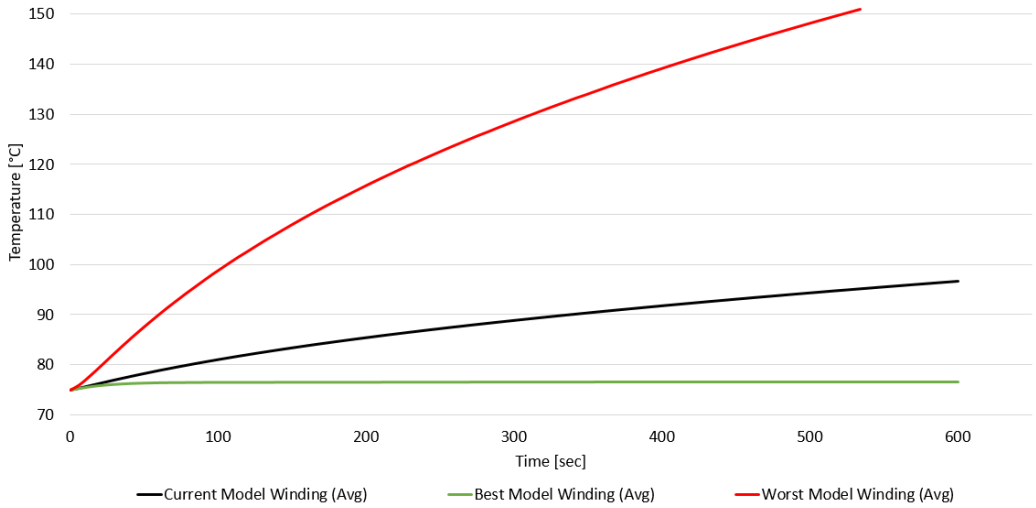

Figure 7. Compared between Current, Best and Worst Model temperature of Winding(Avg).

The cooling jacket temperatures reached about the same degree at the end. In this case, the earlier stages are more important because the cooling jacket temperature should be increased easily at the beginning. This indicates that it absorbs heat faster. The best model reaches 55 °C rapidly after then the temperature curve stabilizes at 55.9 °C. Because of that, 55 °C is chosen as the reference temperature. The best model reaches 55 °C at 138sec while the current model and worst model temperatures are respectively 50.94 °C and 82.86 °C. The best performance increases 7.97% compared to housing jacket outlet temperature at 138 sec.

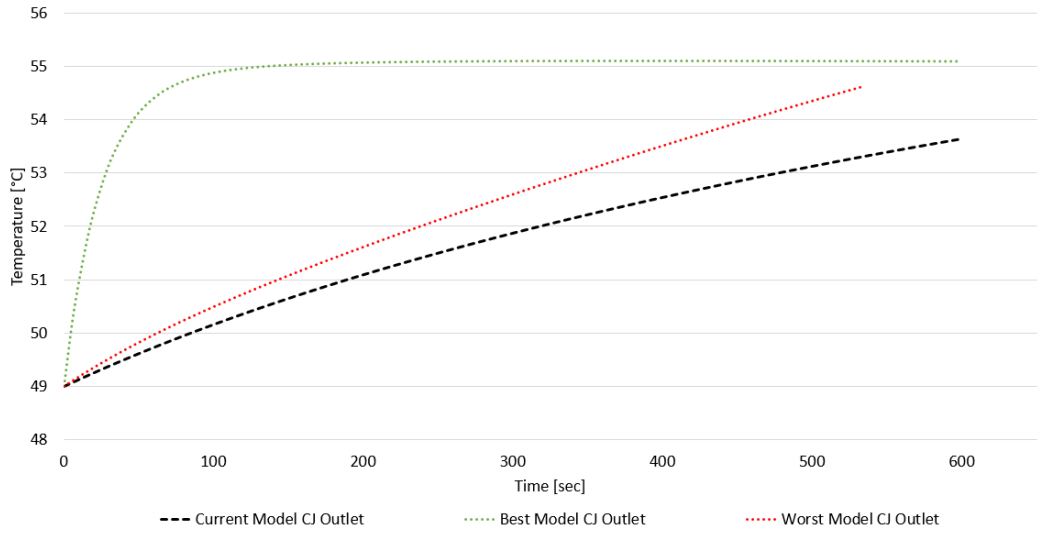

Figure 8. Compared between Current, Best and Worst Model temperature of CJ Outlet.

The best performance increases by 19.39% compared to the winding temperature for the cooling jacket. This improvement results can be seen easily as shown in Figure 6 and Figure 7.

CONCLUSIONS

This study aims to improve the thermal efficiency of a 250 kW permanent magnet synchronous motor over the determined parameters. These parameters are the basic design parameters that make up the cooling jacket. The studied parameters are mass flow rate, pipe diameter, number of turns, fluid types, and torque value. The variables of the parameters are defined as levels, and the best thermal model will create over common usage values.

In order to compare iterations between each other, it is necessary to form combinations of all levels and factors in themselves. In this way, the best result can be achieved. Since there are four levels of each of the five factors, 1024 iterations must be made. The Taguchi method is an L16 orthogonal array that defines the iterations. Thus the iteration numbers decrease to 4^2(16) from 4^5(1024) iterations.

The iterations were analyzed on Ansys and obtained the average winding and cooling jacket temperature results written on the Taguchi analysis table. The Taguchi is based on the minimum average winding temperature in this study. The Taguchi analysis was used as a “smaller is better method” to decrease hot spot temperature on the motor. The hot spot points appear in the motor winding, and the temperature distribution is not equal throughout the winding. Because of that, the data is approved on average. Thus, the best and worst model is acquired by the Taguchi method.

The best thermal model is obtained with these parameters; mass flow rate: 50 l/min, pipe diameter: 17.7 mm, number of turns: 20, type of fluid: EGW 50/50, torque: 2000 Nm. Analysis was performed in Ansys using the best values obtained. As a result of this analysis, changes in the output temperature of the coolant were observed. It reached 55 degrees in 138 seconds. For this reason, the efficiency calculation was made by evaluating the temperature values in 138 seconds. In this stage, the refrigerant efficiency was increased by 7.97%. This way, the PMSMs hot spot temperature decreased to 79°C from 98°C. Due to the improved model, thermal efficiency increased 19.39% with changes only to the cooling jacket.

REFERENCES

[1]. Chiwon Kim, Kwan-Soo Lee , Se-Jin Yook, Effect of air-gap fans on cooling of windings in a large-capacity, high-speed induction motor, ELSEVIER, Applied Thermal Engineering 100 (2016) 658–667.
[2]. Nandy Putra, Bambang Ariantara, Electric motor thermal management system using L-shaped flat heat pipes, ELSEIVER, Applied Thermal Engineering 126 (2017) 1156–1163.
[3]. D. Staton, Mircea Popescu, D. Hawkins, Aldo Boglietti, Influence of different end region cooling arrangements on end-winding heat transfer coefficients in electrical machines, IEEE Xplore October 2010 , DOI:10.1109/ECCE.2010.5617810.
[4]. Staton, D. & Popescu, Mircea & Hawkins, D. & Boglietti, Aldo & Cavagnino, Andrea. (2010). Influence of different end region cooling arrangements on end-winding heat transfer coefficients in electrical machines. 2010 IEEE Energy Conversion Congress and Exposition, ECCE 2010 - Proceedings. 1298 - 1305. 10.1109/ECCE.2010.5617810.
[5]. Xia, Zhengpeng & Zhou, Chenquan & Shen, Dan & Ni, Hongjun & Yuan, Yinnan & Ping, Liao. (2014). Study on the Cooling System of Super-Capacitors for Hybrid Electric Vehicle. Applied Mechanics and Materials. 492. 37-42. 10.4028/www.scientific.net/AMM.492.37.
[6]. Meenen, Jordan. (2010). MIT Electric Vehicle Team Porsche Designing a Cooling System for the AC24 Electric Motor.
[7]. Demetriades, Georgios & Zelaya De La Parra, Hector & Andersson, Erik & Olsson, Hakan. (2010). A Real-Time Thermal Model of a Permanent-Magnet Synchronous Motor. Power Electronics, IEEE Transactions on. 25. 463 - 474. 10.1109/TPEL.2009.2027905.
[8]. Ying Xie, Yunyang Wang, 3D temperature field analysis of the induction motors with broken bar fault, ELSEVIER, Applied Thermal Engineering 66 (2014) 25-34.
[9]. Mokukcu, Mert. (2014). Electric Vehicle Powertrain Design and Implementation.
[10]. Fatih Alpaslan KAZAN1 , Osman BILGIN, Simulation of PMSM Operating at Different Speeds and Optimization of PI Controller Parameters, MAKU-Uyg. Bil. Derg., 4(1), 86-105, 2020.
[11]. Demetriades, G.D., Zelaya, H., Andersson, E., & Olsson, H. (2008). A Real-Time Thermal Model of a Permanent Magnet Synchronous Motor Based on geometrical measures. 2008 IEEE Power Electronics Specialists Conference, 3061-3067.
[12]. Li, Guang-Jin & Ojeda, Javier & Hoang, Emmanuel & Gabsi, Mohamed. (2011). Thermal-Electromagnetic Analysis of a Fault-Tolerant Dual Star Flux-Switching Permanent Magnet Motor for Critical Applications. Electric Power Applications, IET. 5. 503 - 513. 10.1049/iet-epa.2010.0250.
[13]. Chaieb, Mohamed & Naourez, Benhadj & Kammoun, J.K. & Neji, Rafik. (2015). Thermal modeling of permanent magnet motor with finite element method. 594-598. 10.1109/STA.2014.7086733.
[14]. R. Cermak and R. Pechanek, Thermal Study of Permanent Magnet Direct Drive Wheel Motor, 2018 18th International Conference on Mechatronics - Mechatronika (ME), 2018, pp. 1-6.
[15]. A. Kačenka, A. -C. Pop, I. Vintiloiu and D. Fodorean, Lumped Parameter Thermal Modeling of Permanent Magnet Synchronous Motor, 2019 Electric Vehicles International Conference (EV), 2019, pp. 1-6, doi: 10.1109/EV.2019.8892937.
[16]. Kefalas, Themistoklis & Kladas, A.. (2014). Thermal Investigation of Permanent-Magnet Synchronous Motor for Aerospace Applications. Industrial Electronics, IEEE Transactions on. 61. 4404-4411. 10.1109/TIE.2013.2278521.
[17]. Malumbres, Jose & Satrústegui, Marco & Elosegui, Ibon & Ramos, Juan & Martinez-Iturralde, Miguel. (2014). Analysis of relevant aspects of thermal and hydraulic modeling of electric machines. Application in an Open Self Ventilated machine. Applied Thermal Engineering. 75. 10.1016/j.applthermaleng.2014.10.012.
[18]. Yalong Sun, Shiwei Zhang, Wei Yuan, Yong Tanga, Jingrong Li, Kairui Tang, Applicability study of the potting material based thermal management strategy for permanent magnet synchronous motors, ELSEIVER, Applied Thermal Engineering 149 (2019) 1370–1378.
[19]. Johnston, David & Kumar, Nitish & Joshi, Yogendra & Kumar, Satish & Tikadar, Amitav. (2020). Comparison of Electro-Thermal Performance of Advanced Cooling Techniques for Electric Vehicle Motors. Applied Thermal Engineering. 183. 10.1016/j.applthermaleng.2020.116182.
[20]. O. Ustun et al., "Design and manufacture of electric powertrain and its cooling system for ITU EV project," 2014 International Conference on Electrical Machines (ICEM), 2014, pp. 730-735, doi: 10.1109/ICELMACH.2014.6960262.
[21]. Satrústegui, Marco & Martinez-Iturralde, Miguel & Ramos, Juan & Gonzalez, Patxi & Astarbe, Gorka & Elosegui, Ibon. (2016). Design criteria for water cooled systems of induction machines. Applied Thermal Engineering. 114. 10.1016/j.applthermaleng.2016.12.031.
[22]. T. D. Kefalas and A. G. Kladas, "Finite element transient thermal analysis of PMSM for aerospace applications," 2012 XXth International Conference on Electrical Machines, 2012, pp. 2566-2572, doi: 10.1109/ICElMach.2012.6350246.
[23]. Yasar MUTLU,(2011), ELEKTRIKLI ARAC MOTORUNUN SOGUTMA SISTEM TASARIMI.
[24]. A. Apte, R. Walambe, V. Joshi, K. Rathod and J. Kolhe, "Simulation of a permanent magnet synchronous motor using Matlab-Simulink," 2014 Annual IEEE India Conference (INDICON), 2014, pp. 1-5, doi: 10.1109/INDICON.2014.7030469.
[25]. Jebahi, Radhia & Aloui, Helmi & Ayadi, Moez. (2017). One-dimensional Lumped-Circuit for Transient Thermal Study of an Induction Electric Motor. International Journal of Electrical and Computer Engineering (IJECE). 7. 1714. 10.11591/ijece.v7i4.pp1714-1724.
[26]. Ponomarev, Pavel & Polikarpova, M. & Pyrhonen, J.. (2012). Thermal modeling of directly-oil-cooled permanent magnet synchronous machine. Proceedings - 2012 20th International Conference on Electrical Machines, ICEM 2012. 1882-1887. 10.1109/ICElMach.2012.6350138.

[27]. Aziz, Rebaz & Atkinson, G. & Salimin, Suriana. (2017). Thermal Modelling for Permanent Magnet Synchronous Machine (PMSM). International Journal of Power Electronics and Drive Systems (IJPEDS). 8. 1903. 10.11591/ijpeds.v8.i4.pp1903-1912.
[28]. Rehman, Z.; Seong, K. Three-D Numerical Thermal Analysis of Electric Motor with Cooling Jacket. Energies 2018, 11, 92. https://doi.org/10.3390/en11010092.
[29]. Fan, Jinxin & Zhang, Chengning & Wang, Zhifu & Dong, Yugang & Nino, C.E. & Rehman, Abdul & Strangas, Elias. (2010). Thermal Analysis of Permanent Magnet Motor for the Electric Vehicle Application Considering Driving Duty Cycle. Magnetics, IEEE Transactions on. 46. 2493 - 2496. 10.1109/TMAG.2010.2042043.
[30]. Fang, Guoyun & Yuan, Wei & Yan, Zhiguo & Sun, Yalong & Tang, Y.. (2019). Thermal management integrated with three-dimensional heat pipes for air-cooled permanent magnet synchronous motor. Applied Thermal Engineering. 152. 10.1016/j.applthermaleng.2019.02.120.
[31]. Cavazzuti, Marco & Gaspari, Gloria & Pasquale, Stefano & Stalio, Enrico. (2019). Thermal management of a Formula E electric motor: Analysis and optimization. Applied Thermal Engineering. 157. 113733. 10.1016/j.applthermaleng.2019.113733.
[32]. Zhang, Hengliang & Giangrande, Paolo & Sala, Giacomo & Xu, Zeyuan & Hua, Wei & Madonna, Vincenzo & Gerada, David & Gerada, Chris. (2020). Thermal Model Approach to Multisector Three-Phase Electrical Machines. IEEE Transactions on Industrial Electronics. PP. 1-1. 10.1109/TIE.2020.2977559.
[33]. Tauseef, Giasuddin & Chao, Shuo. (2014). Thermal Analysis of PMSM Stator using ANSYS. 10.13140/2.1.4845.1366.
[34]. Wang, Shengnan & Li, Yunhua & Li, Yun-Ze & Wang, Ji-Xiang & Xiao, Xi & Guo, Wei. (2016). Transient cooling effect analyses for a permanent-magnet synchronous motor with phase-change-material packaging. Applied Thermal Engineering. 109. 10.1016/j.applthermaleng.2016.08.036.

ICENS 8TH INTERNATIONAL CONFERENCE ON ENGINEERING AND NATURAL SCIENCE
May 18-22 2022 Istanbul (Hybrid Event)

Comparative Life Cycle Assessment of Metalworking Processes in Shipyards

***Mehmet Onal*[1]**

Abstract

The metalworking process is one of the main processes in a ship's life cycle. Shipyard managers and operators are making a global effort to meet the material processing demands required in shipbuilding while ensuring the system's sustainability. As a method, life cycle assessment (LCA) was applied, which was modeled using LCA software, and the effects of the system were examined based on the CML-IA evaluation method. This method allows for the systematic and scientific calculation of environmental impacts, taking into account all of a system's inputs and outputs and thus aiding in the comparison of options on an environmental basis. LCA is widely used in shipyard management based on the entire maritime system or just a part of it (for example, operation, construction, or recycling). In this study, after briefly mentioning the global examples of LCA, the focus will be on determining the options for improving the sustainability of this system, together with evaluating the environmental impacts of the processing of steel and aluminum materials in the chosen shipyard, an example.

Keywords: LCA, Metalworking, Sustainability

1. INTRODUCTION

Within industries, sustainable development is an accepted concept. On the idea of sustainability, which the United Nations defines as meeting the needs of today without compromising the ability of future generations to meet their needs [1], separate studies are conducted in all processes, from the supply of raw materials to the recovery of materials. Sustainability tools are utilized for design, production, operation/use, recycling, and environmental impact management of the logistics required for all of these processes.

In recycling-oriented production, eco-design has emerged as a crucial aspect of engineering design. With life cycle analysis (LCA), one of the sustainability tools, it is possible to present a cradle-to-grave assessment of an industrial system's environmental impact that considers all of its processes [2], from sourcing raw materials to its recycling. LCA is a tool for making comparisons. In this regard, LCA enables industry decision-makers to compare the differences between their current practices and the environmental impact of their alternative plans.

The cradle-to-grave LCA methodology necessitates a comprehensive data collection procedure. Life cycle assessment requires the most time and resources to create a life cycle inventory (LCI) by collecting product and process data [3]. To reveal the environmental effects of the system's components, it is necessary to determine the system's boundaries and then compare the environmental impacts of the system's stages.

As shown in Table 1, the cradle-to-grave LCA process for a ship includes the procurement of raw materials, construction, operation, and recycling [3]. Each section may be subdivided into lower limits within which an LCA evaluation can be conducted. Ship construction includes metalwork, welding, piping, fittings, paint, machinery, and equipment layout [4].

By establishing the boundaries for the ship life cycle analysis, focus groups are formed. It is possible to improve environmental impact from part to whole by interpreting the results of environmental impacts that occur within these boundaries.

Table 9. Life cycle phases of a ship [4]

[1] *Naval Architecture and Maritime Faculty, Izmir Katip Celebi University, Turkey, mehmet.onal@ikc.edu.tr*

Building	Operation	Recycle
• Metalwork and surface improvement • Welding operations • Pipelines • Equipment • Paint • Main and auxiliary machine	• Fuel consumption • Oil change • Maintenance	• Dismantling • Transport

1.1 Overview of Materials Used in Shipbuilding

The term "mild steel" refers to the type of steel that is most frequently employed in shipbuilding due to its affordability, properties, and availability. This material is suitable for cold and hot forming and welding, and its mechanical properties do not change significantly when subjected to processing temperatures [5]. However, when the temperature drops to deficient levels, the material loses its impact hardness, gains brittleness, and can cause brittle fractures within the body. Before inspecting, testing, and stamping a piece of steel for use [6] in shipbuilding, a classification society must certify the ship [7].

Aluminum alloys [8] used in shipbuilding are referred to as marine aluminum alloys, and they are classified, inspected, and documented similarly to steel material [7]. Despite having yield stress that is nearly identical to that of mild steel, the most notable characteristic of aluminum is that its density is roughly one-third that of steel. On the other hand, aluminum structures weigh roughly half their equivalent steel counterparts. This is due to the fact that aluminum has a significantly lower yield strength than steel [9].

This study compared to steel and aluminum shipbuilding materials for the metal works department.

2. MATERIALS AND METHOD

This study aims to establish an LCA framework for shipyard metalworking processes. This study aims to demonstrate how the framework depicted in Figure 1 can be implemented in shipbuilding. This methodology outlines the primary procedures for the metalworking techniques under consideration.

The required system inputs per ton for aluminum and steel metalworking processes are analyzed in the study. The objective is to compare the environmental effects after processing.

2.1. Life Cycle Assessment

LCA is a knowledge-based comparative tool used for environmental assessment and management of production systems. This comparison will be based on the concept of a functional unit, which represents the quantitative expression of equal payoff for the systems being compared. This procedure is known as "Life Cycle Assessment" because it considers all aspects of a product's life, from conception to eventual disposal. LCA's cradle-to-grave care makes it unique. The life cycle assessment (LCA) has many advantages, especially for the environment. LCA can identify and track tradeoffs, which are the changes in environmental impacts that occur when transitioning from one environment to another or from one stage of a product's life cycle. These modifications can occur when transitioning from one environment to another or from one phase of a product's life cycle to the next. The data used in LCA studies must be meticulously gathered, evaluated, and validated. Consequently, the analysis performed during these studies can be extensive and time-consuming.

Shipyard material processing processes are compared to determine the environmental impact of each tonne unit of material processed shown in Table 2—the study utilized aluminum and steel metalworking information from shipyards and published materials per ton.

The study's findings were analyzed and compared in their Global Warming Potential (GWP). The unit of measure "kgCO_2 Eq" will be utilized for all quantities under GWP impact. CO_2 is the standard component for this type of effect. Each quantity can be converted to standard units by multiplying it by its respective characterization factor. Various scientific communities define variables used to characterize something based on various problem-solving strategies and worldviews regarding environmental issues.

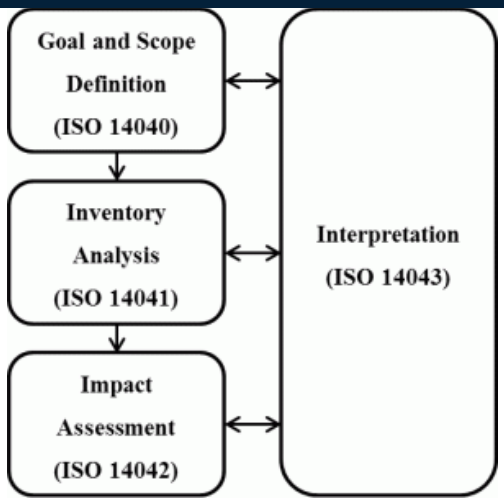

Figure 1 LCA Methodology(ISO 14040:2006) [10]

Table 2 Shipyard Metalworking Inputs

	Process Name	System Inputs
Shipbuilding Metalworking Phase	Steel Metalwork	CO2 O2 LPG Electricity
	Aluminum Metalwork	Argon Electricity

3. RESULTS AND DISCUSSION

As a result of the outcomes of the shipyard operations, the effects of the LCA could be displayed as a comparison of the GWP values. The process comparisons considered for a ton could reveal the metalworking evaluation of the environmental effects of shipyards, which comprise the construction segment of the maritime industry. Aluminum and steel shipyard metalworking processes were compared, and the results are shown in Figure 2.

Only shipyard processes were compared by excluding the significant environmental impact, and the outcomes are shown in Figure 3.

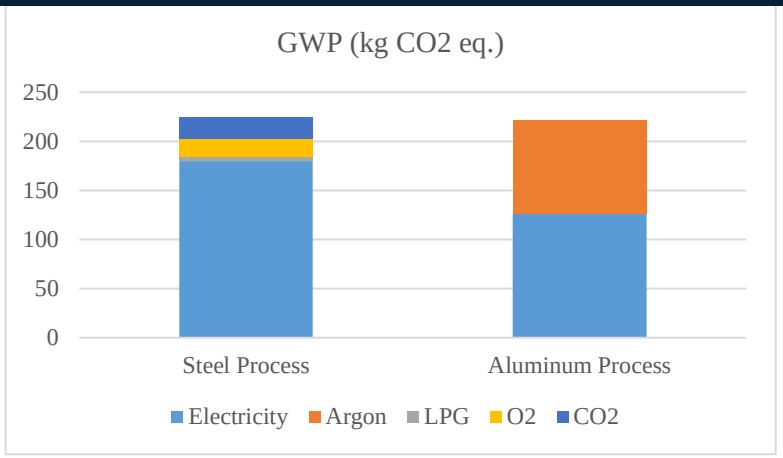

Figure 2 Comparison of shipyard metalworking processes (excluding material effect)

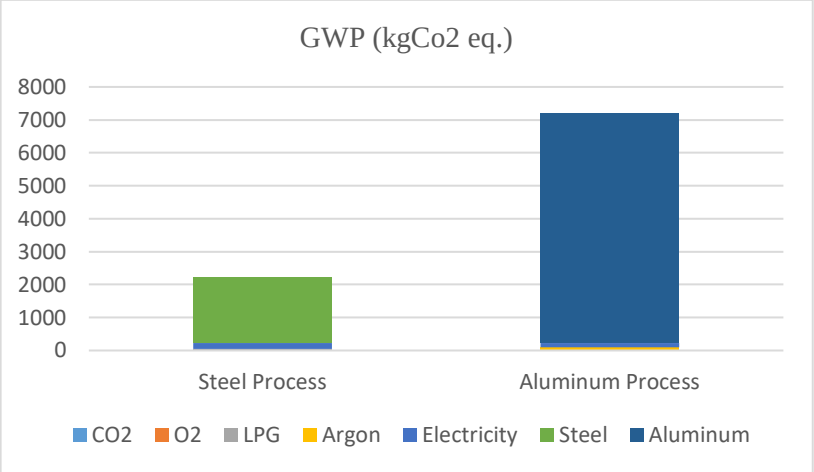

Figure 3 Comparison of shipyard metalworking processes (including material effect)

4. CONCLUSION

When comparing only the environmental impacts of metalworking, excluding the extraction of raw materials, steel processing is found to have slightly greater environmental impacts than aluminum processing.

In a comparison of metalworking processes, it has been observed that the environmental impact of aluminum processing is more significant than that of steel processing when the extraction of the material is factored into the calculation.

The environmental impact of steel processing system inputs accounts for 10% of the total impact. The environmental impact of system inputs accounts for 3 percent of the total impact in aluminum processing.

REFERENCES

[1] United Nations, *Sustainability*. [Online]. Available: https://www.un.org/en/academic-impact/sustainability (accessed: May 15 2022).
[2] M. Onal and G. Neser, "End-of-Life Alternatives of Glass Reinforced Polyester Boat Hulls Compared by LCA," *Advanced Composites Letters*, vol. 27, no. 4, pp. 134–141, 2018.
[3] Ugur Bugra CELEBI, "Generic Naval Vessel Waste Management Model Development In Ship-Life Cycle Assessment (SLCA) And Cost (SLCC)," *Journal of Naval Sciences and Engineering*, vol. 16, no. 2, pp. 193–216, 2020.
[4] M. Onal, G. Neser, and K. T. Gursel, "Environmental impacts of steel ship hulls building and recycling by life cycle assessment (LCA)," *Ships and Offshore Structures*, vol. 16, no. 10, pp. 1061–1066, 2021, doi: 10.1080/17445302.2020.1816706.
[5] Jorge Malave, *Specification for Structural Steel Buildings*, 1989.
[6] L. Gardner, "The use of stainless steel in structures," *Prog. Struct. Engng Mater.*, vol. 7, no. 2, pp. 45–55, 2005, doi: 10.1002/pse.190.
[7] *Chapter 2 – Material*, Turk Loydu Rules, 2021.
[8] W. S. Park, M. S. Chun, M. S. Han, M. H. Kim, and J. M. Lee, "Comparative study on mechanical behavior of low temperature application materials for ships and offshore structures: Part I—Experimental investigations," *Materials Science and Engineering: A*, vol. 528, no. 18, pp. 5790–5803, 2011, doi: 10.1016/j.msea.2011.04.032.
[9] R. A. Sielski, "Research needs in aluminum structure⁎," *Ships and Offshore Structures*, vol. 3, no. 1, pp. 57–65, 2008, doi: 10.1080/17445300701797111.
[10] *Environmental Management — Life Cycle Assessment — Principles and Framework.*, ISO 14040, 2006.

ICENS 8TH INTERNATIONAL CONFERENCE ON ENGINEERING AND NATURAL SCIENCE
May 18-22 2022 Istanbul (Hybrid Event)

Numerical study of heat transfer of a battery pack consisting of plate-shaped lithium-ion batteries connected to the solar system in an air channel in the presence of PCM

Nevzat Akkurt[1]

Abstract

In this paper, heat transfer in a battery pack located in an air duct is studied numerically. Lithium-ion batteries are widely used in electronic devices, and various companies are trying to improve their capacity. One of the problems is their heating during operation. Therefore, in this work, a lithium-ion battery pack in a rectangular case filled with a phase change material (PCM) is numerically investigated. The battery and the PCM enclosure are located in a duct with laminar air flow. This study is performed for Reynolds numbers (Re) of 50 and 250 for one hour. COMSOL Multiphysics software and finite element method are used to solve the governing equations. The results of this study show that as the time increases, the amount of melt PCM around the battery decreases continuously. Re = 250 results in more solid PCM at different times than Re = 50. Also, at Re = 250, the molten PCM is converted to solid PCM in a shorter time. The average temperature of the battery is increased and then decreased over time. In addition, the battery temperature and the trend of increasing the battery temperature decrease with Re. By increasing Re, the temperature of the exhaust air decreases.

Keywords: Solar System, Lithium-Ion Battery, Air-Cooled Method, Plate, Cylindrical

1. INTRODUCTION

Due to the particular advantages of lithium-ion batteries, their use in electric vehicles is now receiving considerable attention. Although these batteries are widely used for low power applications such as cell phones, laptops, and camcorders, one of the main problems in their commercial use for high power applications such as electric vehicles is their heat generation. Ruhani et al [1] studied and simulated the effects of the distance between the batteries and the input and output of an air-cooled battery pack. They used the finite element method and evaluated the performance of the thermal management system of an air-cooled lithium-ion battery. Their results show that using a specific model reduces the battery temperature by 40%. It was also shown that increasing the inlet valve size improves heat transfer and lowers the temperature at the surface of the battery. Zhang et al [2] experimentally studied the toxic effects and ultra-thermal risks of lithium-ion batteries. They measured the internal temperature and voltage of the battery as well as the gases generated during heat dissipation. Their results showed that the internal temperature of the battery is much higher than the surface temperature. Monika and Datta [3] studied different types of channels for cooling lithium batteries. To cool the lithium battery, they used six different channel shapes. According to the results, serpentine and hexagonal shapes can greatly increase the temperature uniformity, although the pumpkin model has less pressure drop and pumping power. Jang et al [4] studied the use of heat pipes in lithium battery cooling. As can be seen, there are many studies on different methods of battery cooling, and different methods have been presented by researchers depending on the application and energy consumption. Baggio [5] studied how heat pump systems and energy storage technologies can be used to cool and heat a building system. Tyagi et al [6] investigated energy storage in buildings.

[1] *Corresponding author:Nevzat Akkurt, Munzur University Department of Mechanical Engineering 62000, Tunceli/Turkey*

Saechan et al [7] performed a numerical analysis of an air-cooled lithium battery thermal management system. They said that the air-cooled thermal management system has minimal manufacturing cost, is easy to set up, and has high system reliability.

Batteries are widely used in the devices of people's daily life. One of their problems is that their temperature rises during operation. Heat generation is higher in batteries with higher capacity and shorter charging time. Therefore, in this work, the cooling of a plate battery cell is simulated by using air flow and PCM. The PCM is located in an enclosure surrounding the battery. The battery and the enclosure are located in an air duct. This study is performed when PCM is fully melted to obtain the most sensitive conditions for the cooling system. The simultaneous use of active and passive methods for thermal management is an innovation of the present work.

2. A PROBLEM DEFINITION AND GOVERNING EQUATIONS

Lithium-ion batteries are packaged in different arrangements depending on heat generation and number of cells. In this study, a lithium-ion battery cell is placed in an enclosure with different shapes. The airflow cools the battery by hitting the battery and the duct and finally exiting the other side.

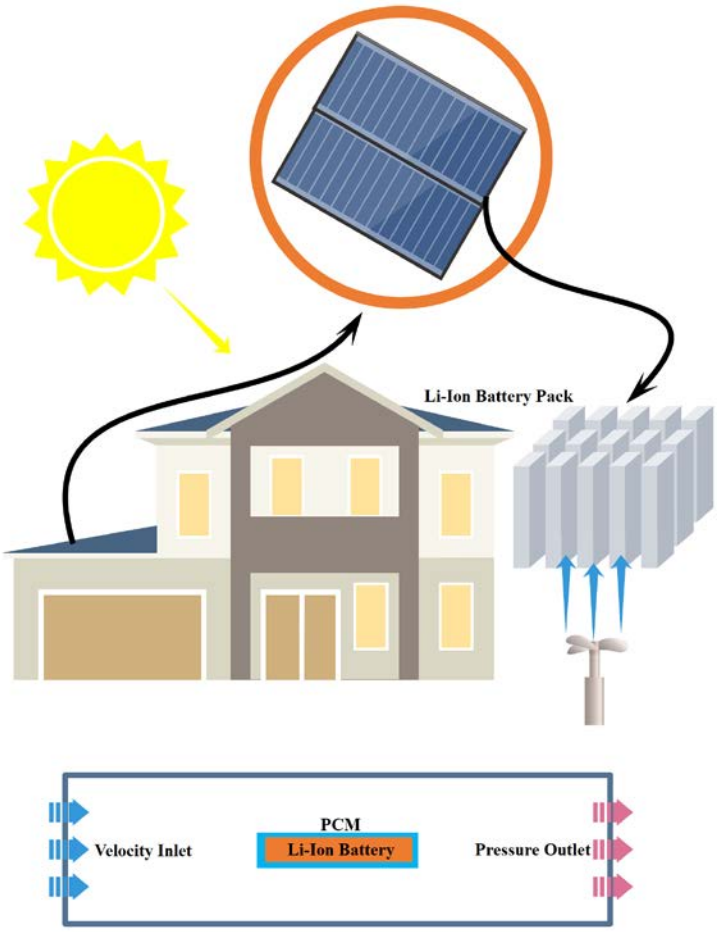

Figure. 1. General schematic of the problem.

The airflow enters the duct at constant temperature and velocity and exits the other side at constant pressure. After solving the battery equations, which appear as source terms in the energy equation, heat is generated inside the battery, causing PCM to melt. The PCM provides a uniform temperature on the surface of the battery.

$$\rho c_p \frac{\partial T}{\partial t} = \frac{\lambda_r}{r}\frac{\partial}{\partial r}\left(r\frac{\partial T}{\partial r}\right) + \frac{\lambda_\varphi}{r^2}\frac{\partial^2 T}{\partial \varphi^2} + \lambda_Z \frac{\partial^2 T}{\partial z^2} + Q \tag{1}$$

Here Q stands for the flux generated in the battery and λ for the thermal conductivity. Also, ρ and c_p stand for density and heat capacity, respectively. Based on the results of Bernardi et al. [8] the amount of heat flux in the battery is defined as follows:

$$Q = I[(U_{OCV} - U) + IT\frac{\partial U_{OCV}}{\partial T}] \tag{2}$$

This equation represents the two types of heat generated in the battery: that generated by Joule resistance and that generated by entropy and electrochemical reaction in the battery. I is the charge and discharge current and U_OCV is the open circuit voltage. Thus, the equation for heat generation in the battery is as follows:

$$q = \frac{I}{V}[(U_{OCV} - U) + T\frac{\partial U_{OCV}}{\partial T}] = \frac{I}{V}\left(IR_j + T\frac{\partial U_{Ocv}}{\partial T}\right) \tag{3}$$

For numerical modelling of the solid-liquid phase transition, the enthalpy-porosity method is used. In this method, the entire computational domain is a porous domain, so the value of the porosity coefficient is equal to one in the liquid phase and zero in the solid phase. The solid-liquid interface forms a mushy region where the porosity coefficient varies between zero and one. In this method, a solid grid is used and the location of the solid-liquid interface is determined implicitly at each time point. The following equations for continuity, momentum, and energy are established:

$$\frac{\partial u}{\partial x} + \frac{\partial v}{\partial y} = 0 \tag{4}$$

$$\rho\left(\frac{\partial u}{\partial t} + u\frac{\partial u}{\partial x} + v\frac{\partial u}{\partial y}\right) = -\frac{\partial p}{\partial x} + \mu(\frac{\partial^2 u}{\partial x} + \frac{\partial^2 u}{\partial y}) + \rho g\beta\, cos(\theta)\,(T - T_m) + Au \tag{5}$$

$$\rho\left(\frac{\partial v}{\partial t} + u\frac{\partial v}{\partial x} + v\frac{\partial v}{\partial y}\right) = -\frac{\partial p}{\partial y} + \mu(\frac{\partial^2 v}{\partial x} + \frac{\partial^2 v}{\partial y}) + \rho g\beta\, sin(\theta)\,(T - T_m) + Av \tag{6}$$

In momentum equations, the term A expresses the porosity function, which refers to the flow in the porous medium:

$$A = -C\frac{(1-\gamma)^2}{\gamma^3 + \varepsilon} \tag{7}$$

where c = 106 is a mushy constant. Also, ε is 10^{-3} to avoid dividing the above fraction by zero when the amount of the liquid fraction is zero. The amount of the liquid fraction is also calculated using the following equation:

$$\gamma = \frac{\Delta H}{L_{sf}} = \begin{cases} 0 & if \quad T < T_{solidus} \\ \frac{T - T_{solidus}}{T_{Liquidus} - T_{solidus}} & if \quad T_{Liquidus} < T < T_{solidus} \\ 1 & if \quad T > T_{Liquidus} \end{cases} \tag{8}$$

Energy conservation equation:

$$\rho\left(\frac{\partial}{\partial t}(c_P T) + \frac{\partial}{\partial x}(c_P u T) + \frac{\partial}{\partial y}(c_P v T)\right) = \frac{\partial}{\partial x}\left(k\frac{\partial T}{\partial x}\right) + \frac{\partial}{\partial y}\left(k\frac{\partial T}{\partial y}\right) - S_T \tag{9}$$

$$S_T = \rho\left(\frac{\partial}{\partial t}(\Delta H) + \frac{\partial}{\partial x}(u\Delta H) + \frac{\partial}{\partial y}(v\Delta H)\right) \quad (10)$$

The equations of motion and continuity are given for a Newtonian fluid. A laminar, incompressible and steady flow is considered. Body forces such as gravity are ignored and a two-dimensional flow is assumed. The continuity equations, the x and y equations are:

$$\frac{\partial u}{\partial x} + \frac{\partial v}{\partial y} = 0 \quad (11)$$

$$\rho\left(u\frac{\partial u}{\partial x} + v\frac{\partial u}{\partial y}\right) = -\frac{\partial p}{\partial x} + \mu\left(\frac{\partial^2 u}{\partial x^2} + \frac{\partial^2 u}{\partial y^2}\right) \quad (12)$$

$$\rho\left(u\frac{\partial v}{\partial x} + v\frac{\partial v}{\partial y}\right) = -\frac{\partial p}{\partial y} + \mu\left(\frac{\partial^2 v}{\partial x^2} + \frac{\partial^2 v}{\partial y^2}\right) \quad (13)$$

3. NUMERICAL METHOD AND VALIDATION

The finite element approach is used to algebraize the equations regulating the airflow in the duct. The current simulations are validated using the results of Wang et al [9]. Using an air-cooled system, they investigated the battery thermal management system. They tested different layouts and obtained results with different input and output configurations. They introduced the Z-model for battery thermal management and showed that it outperformed previous models by lowering the maximum battery temperature from 3.42 to 6.4 K. 2. As a result, the highest temperature is compared. Figure 2 shows that using the current model gives satisfactory results with a maximum inaccuracy of 1.93 percent. Therefore, this model is used as a criterion for the simulations.

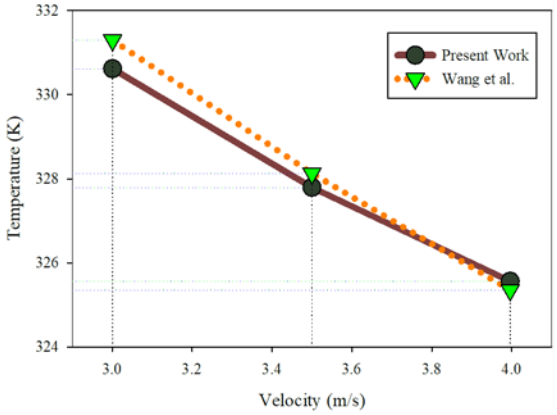

Figure. 2. Maximum temperature generated at the battery as a function of air velocity at the inlet of the battery pack. The data are from the present work and were reported by Wang et al [9].

Table 1 shows that almost the same results are obtained for finer grids than 135552. Therefore, an unstructured grid with 135552 elements is chosen to reduce the computation time. The grid has triangular elements and is better distributed in the areas where there are PCM and in the areas where the airflow meets the angles of the accumulator.

Table 1. Maximum temperature calculated on the battery surface and pressure drop within the channel for different grids.

Grid		99874	103228	118664	135552	143221
	T_{max}	305.020	306.520	307.234	307.334	307.334
	ΔP	160.211	163.011	164.221	165.55	165.55

4. RESULTS AND DISCUSSION

Figure. 3 shows the PCM melting contours up to one hour for Re = 50 and 250. When air hits the case of PCM, some of the heat stored in PCM is released to the air. This causes the molten PCM to become a solid PCM. Therefore, some of PCM solidifies in the battery pack. As more air impinges over time, more heat is removed from PCM, making it more solid PCM. As the battery also operates in this mode, it generates a certain amount of heat. This heat is transferred to the air along with the heat stored in the PCM. At Re = 50, more time is required to transfer the stored heat of the battery to the air. The process of converting molten PCM to solid PCM takes more time, and after 1 hour, a significant portion of PCM is still liquid. But at Re = 250, where the air velocity is slightly higher, it can absorb the heat stored in PCM in a shorter time. As a result, the liquid PCM is converted to the solid form PCM in a shorter time and a larger amount of PCM is solidified around the battery.

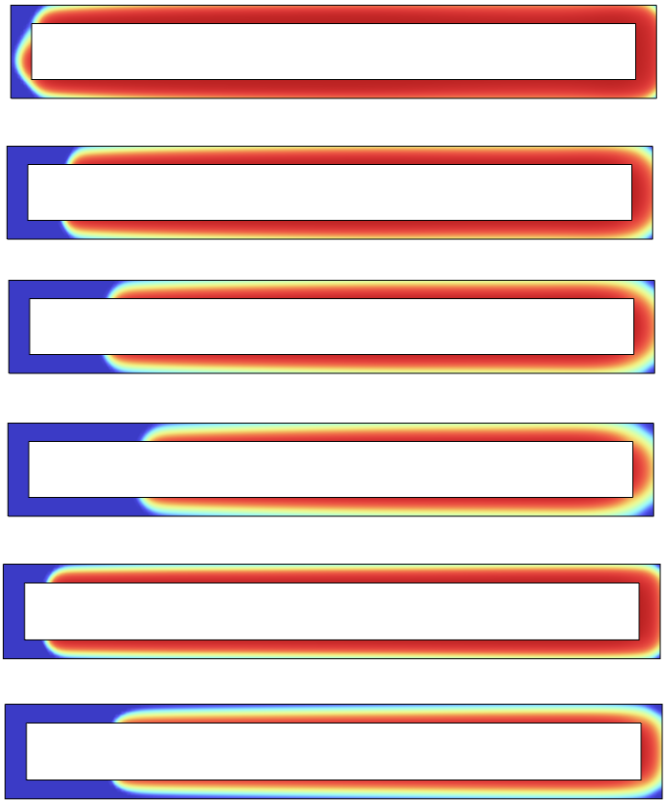

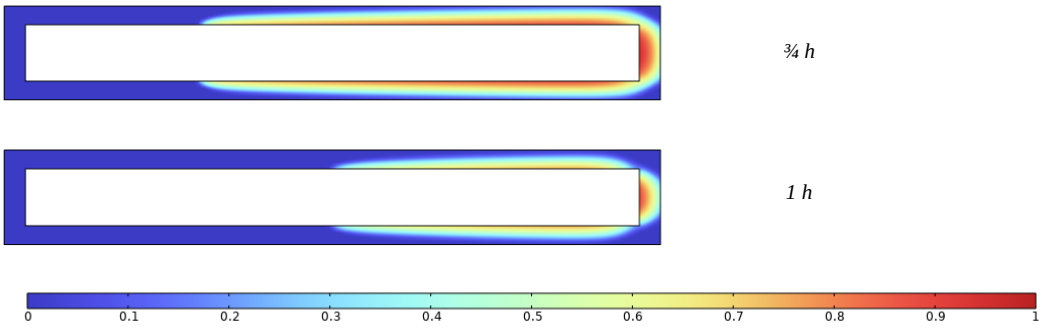

Figure. 3. PCM melting contours up to one hour for Re = 50 and 250.

The average temperature of the accumulator for up to one hour is shown in Fig. 4 for Re = 50 and 250 is shown. The average temperature of the battery is initially elevated and then decreases. Since constant heat is generated in the battery at different times, this heat is dissipated from the battery so that the temperature of the battery does not increase. On the other hand, the battery is 100% melted PCM. Therefore, the air simultaneously absorbs the heat generated in the battery and some of the energy stored in the PCM. Since all parts of the battery are surrounded by molten PCM, the heat transfer between the battery and the air is initially low, so some of the heat generated in the battery is used to heat the battery. However, the temperature of the battery decreases with the solidification of part of PCM and better heat transfer between the battery and the air. The level of Re is very influential during the time that the battery temperature is increased. At Re = 250, where the air velocity is 5 times higher than at Re = 50, the increasing trend of the average temperature of the battery ends and its decreasing trend begins. Moreover, the average temperature of the battery at Re = 250 is slightly lower than at Re = 50.

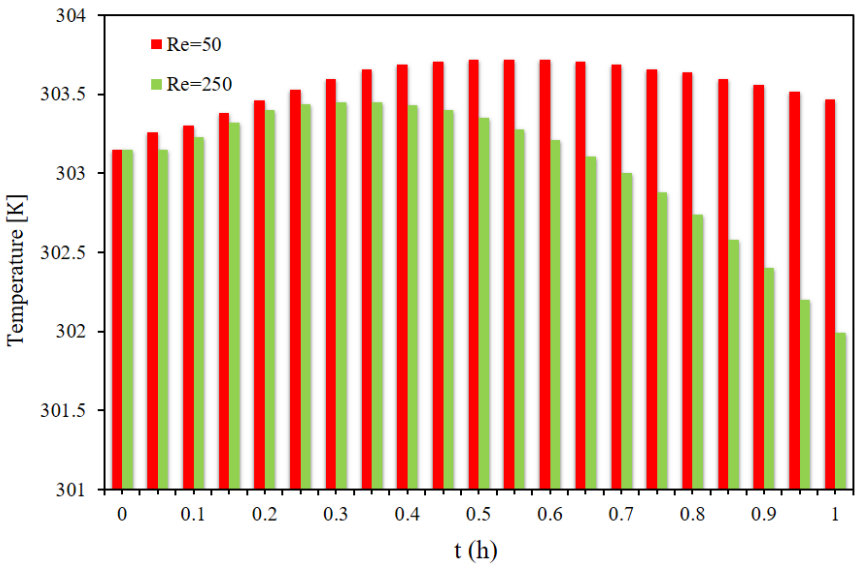

Figure. 4. The average temperature of the battery for up to one hour for Re = 50 and 250.

At Re = 50 and 250, fig. 5 shows the air temperature at the outlet for up to one hour. The temperature of the exhaust air is strongly dependent on Re. The temperature of the exit air generally decreases with time. As a result, the air temperature decreases with time. The increase in air temperature is caused by the heating of the battery and the release of molten PCM

into the air. The amount of melted PCM decreases over time, and as a result, the amount of energy stored in PCM also decreases. One of the causes of heating of the air near the discharge is the transfer of this stored energy to the air. The amount of heat transferred from PCM to the air decreases as the amount of energy stored in PCM decreases, resulting in a decrease in the temperature of the discharge air. Increasing Re decreases the amount of air exiting due to the increase in air velocity in the duct. The faster the air moves through the duct, the longer the air is in contact with the battery and consequently heats up less. The temperature of the air decreases as the speed of the air increases.

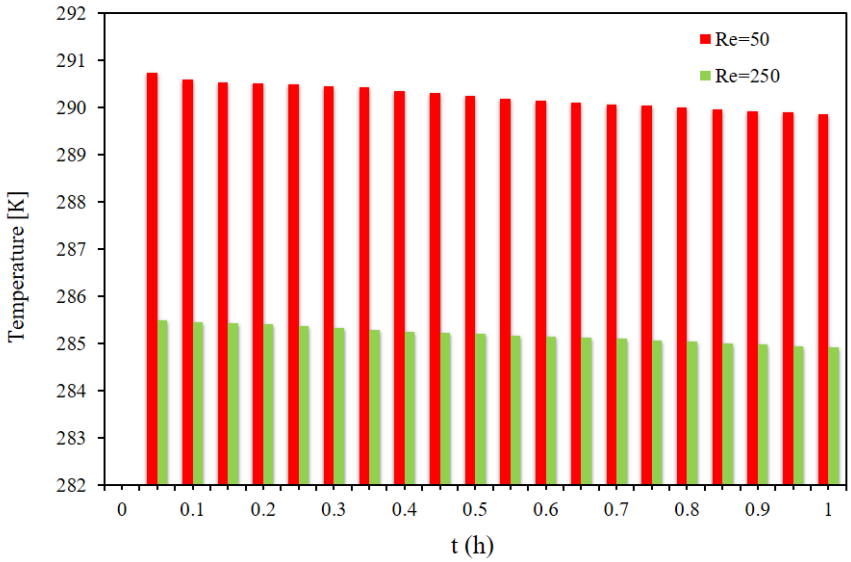

Figure. 5. The air temperature at the outlet for up to one hour at Re = 50 and 250.

The amount of melted PCM for up to one hour at Re = 50 and 250 is shown in Fig. 6. The initial concentration of molten PCM is 100 percent. The amount of liquid PCM decreases with time, while the value of solid PCM increases. When air blows into the PCM container, some of the heat stored in the PCM is released to the air, causing some of the PCM to freeze. The more heat dissipated from the PCM, the more solid PCM there is. As air velocity increases, more energy is stored in the PCM and released to the air in a shorter time, resulting in less molten PCM. As a result, the amount of solid PCM is always slightly greater at Re = 250 than at Re = 50.

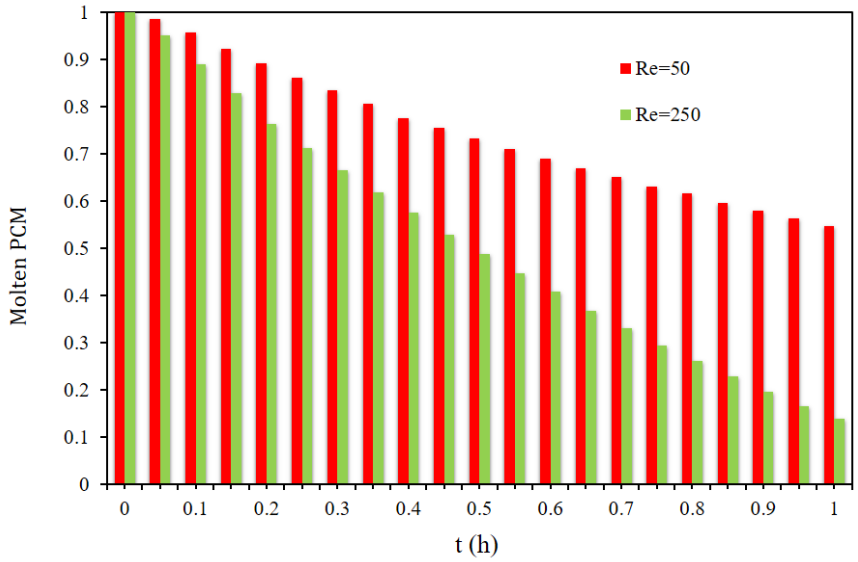

Figure. 6. The amount of molten PCM for up to one hour at Re = 50 and 250.

CONCLUSIONS

In this work, a plate-type lithium-ion battery is simulated, contained in a rectangular enclosure filled with PCM. The battery and the PCM enclosure are mounted in a duct with laminar air flow. At Re = 50 and 250, the battery temperature, outlet air temperature and solid PCM are estimated for up to one hour. The results of this study show:

1- The PCM solidification front occurs at the air inlet side and moves toward the air outlet in the PCM case. The temperature of the battery in the parts connected to the solid PCM is lower.
2- The temperature of the battery is initially increased and then decreased over time. Increasing Re causes the process of increasing the temperature of the battery to decrease in a shorter time. Also, the temperature of the battery is lower with a higher value of Re.
3- The temperature of the air exiting the duct decreases steadily over time. When Re increases from 50 to 250, the temperature of the exiting air decreases.
4- The amount of molten PCM surrounding the battery decreases over time, while the amount of solid PCM increases. Increasing Re increases the amount of solid PCM and causes the entire PCM to solidify in less time.

REFERENCES

[1]. B. Ruhani, A. Abidi, A.K. Hussein, O. Younis, M. Degani, M. Sharifpur, Numerical simulation of the effect of battery distance and inlet and outlet length on the cooling of cylindrical lithium-ion batteries and overall performance of thermal management system, Journal of Energy Storage, 45 (2022) 103714.

[2]. L. Zhang, Q. Duan, X. Meng, K. Jin, J. Xu, J. Sun, Q. Wang, Experimental investigation on intermittent spray cooling and toxic hazards of lithium-ion battery thermal runaway, Energy Conversion and Management, 252 (2022) 115091.

[3]. K. Monika, S.P. Datta, Comparative assessment among several channel designs with constant volume for cooling of pouch-type battery module, Energy Conversion and Management, 251 (2022) 114936.

[4]. D.S. Jang, S. Yun, S.H .Hong, W. Cho, Y. Kim, Performance characteristics of a novel heat pipe-assisted liquid cooling system for the thermal management of lithium-ion batteries, Energy Conversion and Management, (2021) 115001.

[5]. M. Pinamonti, P. Baggio, Energy and economic optimization of solar-assisted heat pump systems with storage technologies for heating and cooling in residential buildings, Renewable Energy, 157 (2020) 90-99.

[6]. V.V. Tyagi, K. Chopra, B. Kalidasan, A. Chauhan, U. Stritih, S. Anand, A.K. Pandey, A. Sari ,R. Kothari, Phase change material based advance solar thermal energy storage systems for building heating and cooling applications: A prospective research approach, Sustainable Energy Technologies and Assessments, 47 (2021) 101318.

[7]. P. Saechan, I. Dhuchakallaya, Numerical study on the air-cooled thermal management of Lithium-ion battery pack for electrical vehicles, Energy Reports, 8 (2022) 1264-1270.

[8]. D. Bernardi, E. Pawlikowski, J. Newman, A General Energy Balance for Battery Systems, Journal of The Electrochemical Society, 132 (1985) 5-12.

[9]. M. Wang, S. Teng, H. Xi, Y. Li, Cooling performance optimization of air-cooled battery thermal management system, Applied thermal engineering, (2021) 117242.

ICENS

8TH INTERNATIONAL CONFERENCE ON ENGINEERING AND NATURAL SCIENCES

CSUN. University of CINCINNATI. IUS. TURKISH AIRLINES. EUROPE CONGRESS www.europecongress.org. CNR GROUP